Yolk-shell electron-rich Ru@hollow pyridinic-N-doped carbon nanospheres with tunable shell thickness and ultrahigh surface area for biomass-derived levulinic acid hydrogenation under mild conditions

Jingsong Yang [1], Ruidong Shi [1], Xiaoxin Xu, Yuanting Li, Xue Wang, Gongbing Zhou [*]

Chongqing Key Laboratory of Green Catalysis Materials and Technology, College of Chemistry, Chongqing Normal University, Chongqing 401331, PR China

ARTICLE INFO

ABSTRACT

Aiming to efficiently upgrade renewable biomass-derived levulinic acid (LA) into γ-valerolactone (GVL), we have devised yolk-shell electron-rich Ru@hollow pyridinic-N-doped carbon nanospheres, featuring a tunable shell thickness (20−70 nm) and an ultrahigh surface area (4016 m^2 g^{-1}). Experimental and theoretical investigations reveal that the strategic formation of the yolk-shell structure and appropriate thinning of the carbon shell facilitate the generation of electron-rich Ru^0 and a positive shift of the *d*-band center towards the Fermi level by increasing surface pyridinic-N species. These modifications suitably intensify Ru^0−H interaction, promote reactant adsorption, stimulate electron transfer between active H and the C═O group of LA, and ultimately reduce apparent activation energy. Consequently, a high LA turnover frequency (18733.4 h^{-1} at 30 °C) and GVL selectivity (99.9%), alongside excellent stability up to eight cycles, are achieved, markedly outperforming externally-supported analogues. These findings afford valuable insights into designing yolk-shell nanostructures for biomass upgrading through microenvironment engineering.

1. Introduction

Hollow yolk-shell-structured nanocatalysts, characterized by void-confined metal nanoparticles (NPs) within porous shells, possess unique features including a large surface area for active site creation, low density, excellent loading capacity, enhanced light scattering, and outstanding resistance to sintering [1]. Importantly, the microenvironment of these nanoarchitectures can be facilely manipulated by tailoring their structural parameters at the nanoscale, such as modulating void-confinement effect [2], precisely locating active sites [3], anchoring ligands near catalytic active centers [4], improving metal-support contact [5], and controlling the yolk or shell size and shape [6]. These modifications lead to improved catalytic behaviors. For instance, Pt@MnO$_x$ [7], Pt@C [8], Pd@SiO$_2$ [9], and Ni@NiAl$_2$O$_4$ [10] yolk-shell catalysts demonstrate superior hydrogenation performances to corresponding crushed or supported ones. Similar enhancements in catalytic behaviors of internally-encapsulated-metal NPs compared to externally-supported analogues appear on Ru@hollow carbon spheres [2,5], PdCu@hollow carbon spheres [11], and Ni@silicate hollow spheres [12].

Metal@hollow carbon nanoarchitectures, among various yolk-shell nanostructures (YSNs), have been extensively studied due to their adjustable chemical composition, controllable mass transfer rates, and excellent acid resistance [13–17]. However, facile optimization of the electronic and geometrical configurations of internally-encapsulated metal active centers by tailoring the microenvironment, especially the outer carbon shell thickness and doped heteroatoms, so as to boost their intrinsic catalytic ability and stability, still remains challenging. At present, three strategies have been developed for constructing YSNs: hard-templating, soft-templating, and self-templating methods, with the hard-templating approach being the most commonly used due to its simplicity, effectiveness, and straightforwardness [1]. Although this strategy has achieved maturity in creating various carbon shell-based YSNs, such as Pd-encapsulated hollow porous carbon nanospheres [18], CoNi alloy-encapsulated carbon nanotube hollow nanocages [19], Zn$_4$Co$_1$O$_x$@carbon hollow capsules [20], and multi-shelled hollow carbon nanospheres [21], further improvement in the catalytic theory of metal@hollow carbon nanoreactors is warranted.

Owing to diminishing fossil fuel reserves and escalating demand for fine chemicals and energy, urgent attention is needed to develop

---

* Corresponding author.
E-mail address: gbzhou@cqnu.edu.cn (G. Zhou).
[1] These authors contributed equally to this work

sustainable alternatives by upgrading renewable lignocellulosic biomass. Among various upgrading routes, selective conversion of cellulose-derived LA to GVL is significant due to the wide-ranging applications of GVL as a gasoline blender, energy-dense fuel additive, biorefining solvent, and intermediate for many chemicals [22–26]. Two probable reaction routes, C=O hydrogenation-intramolecular esterification and cyclization-hydrogenation, have been proposed for the LA-to-GVL process (Scheme S1 in Supplementary Material) [27], with the hydrogenation efficiency determined by active metal [27]. Therefore, optimizing the electronic and geometrical features of metal catalysts is pivotal for promoting the LA-to-GVL conversion. Recent developments have led to the synthesis of yolk-shell nanocatalysts for selective hydrogenation of LA to GVL, including Ru@hollow carbon spheres [2,5], Co@hollow carbon spheres with tailored Co nanoparticle/single-atom ratios [28], Ni-Co phosphides [29], and Ru_1/Fe_3O_4@hollow periodic mesoporous organosilica spheres [30], which exhibited promising behaviors. Nevertheless, the catalytic investigations of YSNs in the LA-to-GVL process are insufficient compared to other hydrogenation reactions, necessitating further elucidation of their intrinsic mechanism for enhancing catalytic ability.

Herein, yolk-shell electron-rich Ru@hollow pyridinic-N-doped carbon (Ru@HNC) nanospheres with easily adjustable shell thicknesses, variable pyridinic-N contents, and ultrahigh surface area are designed, aiming to efficiently upgrade LA into GVL. Through systematic characterizations, kinetics study, density functional theory (DFT) calculations, and Mulliken population analysis, the pivotal roles of the yolk-shell nanostructure and pyridinic-N species on Ru@HNC in the LA-to-GVL process are recognized, and the correlation between catalyst structure and catalytic behaviors is elucidated. Definitive evidences for the formation mechanism of yolk-shell electron-rich Ru@HNC nanostructures and their contributing pathway to improved selective hydrogenation performances are identified.

2. Experimental section

The yolk-shell Ru@HNC catalysts with different shell thicknesses were fabricated using a hard-templating method, which involves deposition, coating, carbonization, etching, and reduction steps (Route A in Fig. 1). In view of the distinct advantages of phenolic resin encapsulation in shell creation, such as high carbon yield, precise control over shell thickness, compatibility with a wide range of active metals, and scalability potential [31], this approach was employed to create carbon shell.

2.1. Preparation of NH_2-modified silica nanospheres

NH_2-modified silica nanospheres were synthesized to serve as a template. SiO_2 nanospheres were obtained by mixing $NH_3 \cdot H_2O$ (9 mL) with a solution of ethanol (16 mL) and H_2O (25 mL), followed by the addition of another mixture consisting of ethanol (45.5 mL) and tetraethyl orthosilicate (TEOS, 4.5 mL). The resulting mixture was stirred for 20 h. The SiO_2 nanospheres were then separated via centrifugation, washed successively with H_2O, acetone, and ethanol, and finally dried at 60 °C overnight.

To modify the obtained SiO_2 nanospheres with $-NH_2$ groups, the product (0.6 g) was dispersed in toluene (40 mL) by sonicating for 10 min. Subsequently, 3-aminopropyltriethoxysilane (APTES, 3 mL) was added, and the mixture was sonicated for another 30 min, followed by stirring for 20 h. The resulting product was collected by centrifugation, washed with toluene and ethanol, and dried at 60 °C for 3 h.

2.2. Deposition of RuO_2 NPs on NH_2-modified SiO_2 nanospheres

The NH_2-modified SiO_2 nanospheres (0.3 g) were dispersed ultrasonically in H_2O (40 mL), followed by the addition of $RuCl_3$ aqueous solution (9.16 mmol L^{-1}, 20 mL), and stirring for 3 h. The resulting solid was isolated and dispersed again in H_2O (30 mL). The suspension
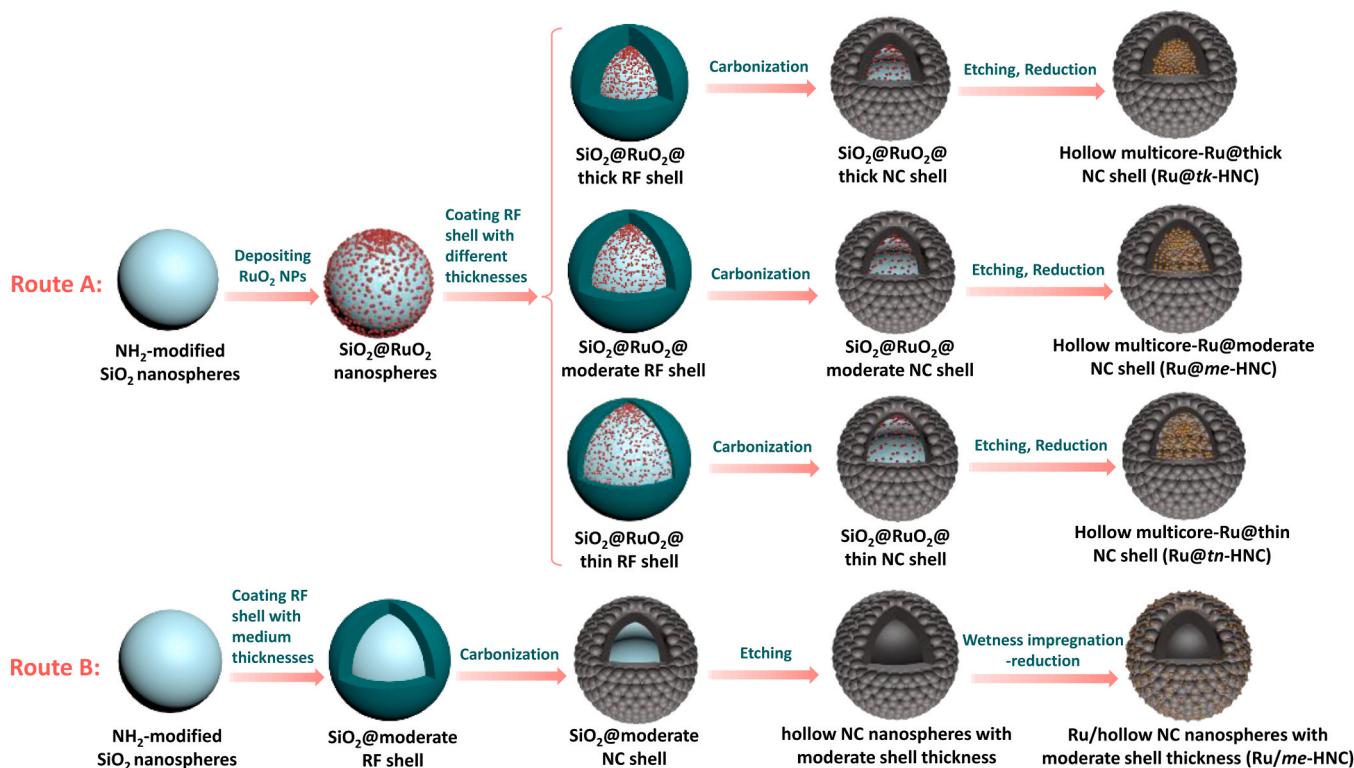

Fig. 1. Synthetic routes of yolk-shell Ru@hollow pyridinic-N-doped carbon nanospheres with thick, moderate, and thin shell thicknesses (route A) and externally supported Ru/*me*-HNC catalyst (route B).

was placed in a 50 mL Teflon-lined autoclave and hydrothermally treated at 150 °C for 16 h. The product (SiO$_2$@RuO$_2$ nanospheres) was isolated via centrifugation, washed with H$_2$O and ethanol, and dried at 60 °C for 3 h. Two batches of SiO$_2$@RuO$_2$ nanospheres were prepared for the next step.

2.3. Coating SiO$_2$@RuO$_2$ nanospheres with resorcinol-formaldehyde (RF) resin of different thicknesses

To coat SiO$_2$@RuO$_2$ nanospheres with a thick RF resin shell (SiO$_2$@RuO$_2$@thick RF shell), the obtained SiO$_2$@RuO$_2$ nanospheres (0.4 g) were dispersed in a solution containing NH$_3$·H$_2$O (2 mL) and ethanol (50 mL) at 33 °C. Another solution composed of ethanol (25 mL), cetyltrimethyl ammonium bromide (CTAB, 0.5 g), resorcinol (0.6 g), and TEOS (0.45 mL) was added, followed by addition of formaldehyde (1.125 mL). The mixture was stirred for 22 h. The obtained dark product was purified with acetone and ethanol, then dried at 60 °C for 3 h.

For coating SiO$_2$@RuO$_2$ nanospheres with moderate and thin RF resins (SiO$_2$@RuO$_2$@moderate RF shell and SiO$_2$@RuO$_2$@thin RF shell), the procedure was identical, except the amounts of resorcinol and formaldehyde were adjusted to 0.4 g/0.75 mL and 0.2 g/0.375 mL, respectively.

2.4. Formation of yolk-shell Ru@HNC catalysts with different shell thicknesses

The obtained SiO$_2$@RuO$_2$@RF was carbonized at 850 °C in Ar (99.999%) for 2.5 h with a heating rate of 5 °C min^{-1}. Subsequently, it was dispersed in HF (20%, 20 mL) and stirred for 1.5 h to etch SiO$_2$. After washing with H$_2$O until neutral, the solid was dried at 60 °C for 3 h and reduced by 5%H$_2$/Ar at 300 °C for 2 h, with a heating rate of 1 °C min^{-1}. According to the use of SiO$_2$@RuO$_2$@thick RF shell, SiO$_2$@RuO$_2$@moderate RF shell, and SiO$_2$@RuO$_2$@thin RF shell, the final yolk-shell Ru@HNC catalysts are denoted as Ru@*tk*-HNC, Ru@*me*-HNC, and Ru@*tn*-HNC, respectively. Here, "*tk*-HNC", "*me*-HNC", and "*tn*-HNC" represent thick, moderate, and thin hollow pyridinic-N-doped carbon shells, respectively.

2.5. Synthesis of externally supported Ru/me-HNC catalyst

The comparative externally-supported Ru/*me*-HNC catalyst was synthesized using a wetness impregnation-reduction method (Route B in Fig. 1). The procedure for synthesizing bare *me*-HNC is identical to that of the Ru@*me*-HNC catalyst, except for omitting the deposition of RuO$_2$ NPs and the reduction at 300 °C under 5%H$_2$/Ar. After obtaining bare *me*-HNC, 0.0531 g of *me*-HNC was dispersed in H$_2$O (10 mL), followed by addition of RuCl$_3$·H$_2$O aqueous (5.61 mmol L^{-1}, 10 mL) and stirring for 2.5 h. The Ru loading (9.6 wt%) and catalyst mass (58.8 mg) were kept identical to Ru@*me*-HNC. The mixture was then directly dried at 60 °C overnight and reduced by 5%H$_2$/Ar at 300 °C for 2 h using a heating rate of 1 °C min^{-1}. The comparative Ru/active carbon (Ru/AC) catalyst was prepared using identical steps as Ru/*me*-HNC, except for replacing *me*-HNC with commercial active carbon.

The details of characterizations, Ru loading calculations, and DFT simulations are provided in the Supplementary Material.

2.6. Catalytic testing

To compare the catalytic performances of different catalysts, the moles of metallic Ru on different catalysts are kept identical at 56 µmol for each catalytic run. For each catalytic run, the as-synthesized Ru@*tk*-HNC (60.1 mg), Ru@*me*-HNC (58.8 mg), Ru@*tn*-HNC (57.8 mg), Ru/*me*-HNC (58.8 mg), or Ru/AC (58.8 mg) catalysts and LA aqueous solution (0.5 mol L^{-1}, 20 mL) were placed in a 50 mL autoclave. Air was replaced with pure H$_2$ (99.999%), and the reaction conditions were

adjusted to 30 °C, 1.0 MPa, and 1600 rpm to initiate the reaction. The reaction mixture was sampled at intervals and quantitatively analyzed using gas chromatograph.

The details for calculating the initial weight-specific activity (r_0) and turnover frequency (TOF) of LA, as well as the stability testing procedure, are provided in the Supplementary Material. Throughout the entire reaction course, GVL is the sole product, demonstrating a GVL selectivity of 99.9%.

3. Results and discussion

3.1. Texture of yolk-shell Ru@HNC and supported Ru/me-HNC

In Fig. 2a, Ru@*tk*-HNC, Ru@*me*-HNC, Ru@*tn*-HNC, and Ru/*me*-HNC exhibit a broad X-ray diffraction (XRD) peak at 2θ of 21.0°, attributed to graphite (002) diffraction (JCPDS: 26–1079), and a weak peak at 2θ of 43.9°, corresponding to metallic Ru (101) diffraction (JCPDS: 06–0663). These findings indicate the successful carbonization of the RF resin layer into graphite carbon and the reduction of RuO$_2$ to metallic Ru. The absence of the peak at 2θ of 43.9° on bare *me*-HNC further confirms the assignment of Ru, and the diffusion feature of Ru diffraction suggests its high dispersion. Additionally, the shift of the graphite (002) line to a lower diffraction angle compared to the standard lines may be attributed to local positive fluctuations in interlayer spacing [32].

In Fig. 2b, the Raman spectra of Ru@HNC and Ru/*me*-HNC are depicted. The gradual attenuation of the peaks observed on Ru@*tk*-HNC, Ru@*me*-HNC, and Ru@*tn*-HNC may be attributed to a decrease in the amount of unorganized carbon and a reduction of graphitic carbon atoms available for Raman scattering per unit volume, resulting from the gradual thinning of the carbon shell [33]. Following Lorentzian deconvolution, three peaks at 1341, 1535, and 1596 cm^{-1} are identified on the four catalysts. These peaks correspond to structural-disordered carbon induced A$_{1g}$ breathing mode (D band), amorphous carbon or interstitial defects (D″ band), and ordered graphitic carbon induced E$_{2g}$ vibration mode (G band), respectively [34]. The intensity ratio of the D to G bands (R value) is widely accepted as an indicator of graphitization degree and alignment of graphitic planes. A lower R value indicates a higher proportion of sp^2-graphite clusters [34]. Based on the deconvoluted integral intensities of the D and G bands, the R values of Ru@*tk*-HNC, Ru@*me*-HNC, Ru@*tn*-HNC, and Ru/*me*-HNC are calculated to be 3.41, 3.58, 3.64, and 3.52, respectively. These similar R values manifest a comparable degree of graphitization among the four catalysts, consistent with the carbonization conditions.

In Fig. 2c–d, the Ru@*tk*-HNC, Ru@*me*-HNC, Ru@*tn*-HNC, and Ru/*me*-HNC catalysts, along with bare *me*-HNC material, all display a type IV isotherm accompanied by a H3 hysteresis loop and a most probable pore size of 3.5 nm. Notably, in Fig. 2c, the adsorbed volume of N$_2$ on Ru@*tn*-HNC is significantly higher than on other catalysts. Consequently, the specific surface area (S_{BET}) and pore volume (V_{pore}) of Ru@*tn*-HNC are highest at 4016 m^2 g^{-1} and 5.78 cm^3 g^{-1} among the four catalysts (Table S1), surpassing the reported S_{BET} of hollow carbon nanospheres (3022 m^2 g^{-1}) [35]. Table S1 further demonstrates that a thinner carbon shell contributes to the increments in S_{BET}, V_{pore}, and average pore diameter (d_{pore}), with the yolk-shell structure enabling a higher S_{BET} compared to the corresponding supported catalyst and bare *me*-HNC. Additionally, the Ru@*tk*-HNC, Ru@*me*-HNC, Ru@*tn*-HNC, and Ru/*me*-HNC catalysts exhibit comparable Ru loadings within the range of 9.4−9.8 wt%, as determined by inductively coupled plasma-atomic emission spectroscopy (ICP–AES, Table S1), an effective technic for measuring Ru loadings of Ru@N-doped carbon catalysts [36–38]. The Ru dispersion slightly decreases with the thinning of the carbon shell, and the internally encapsulated Ru catalyst (Ru@*me*-HNC) has a slightly lower dispersion than the corresponding externally supported one (Ru/*me*-HNC). The variation in Ru dispersion may be caused by two factors, i.e., slower reduction kinetics of pre-loaded RuO$_2$ NPs due to enhanced interaction between RuO$_2$ and a thinner carbon shell as
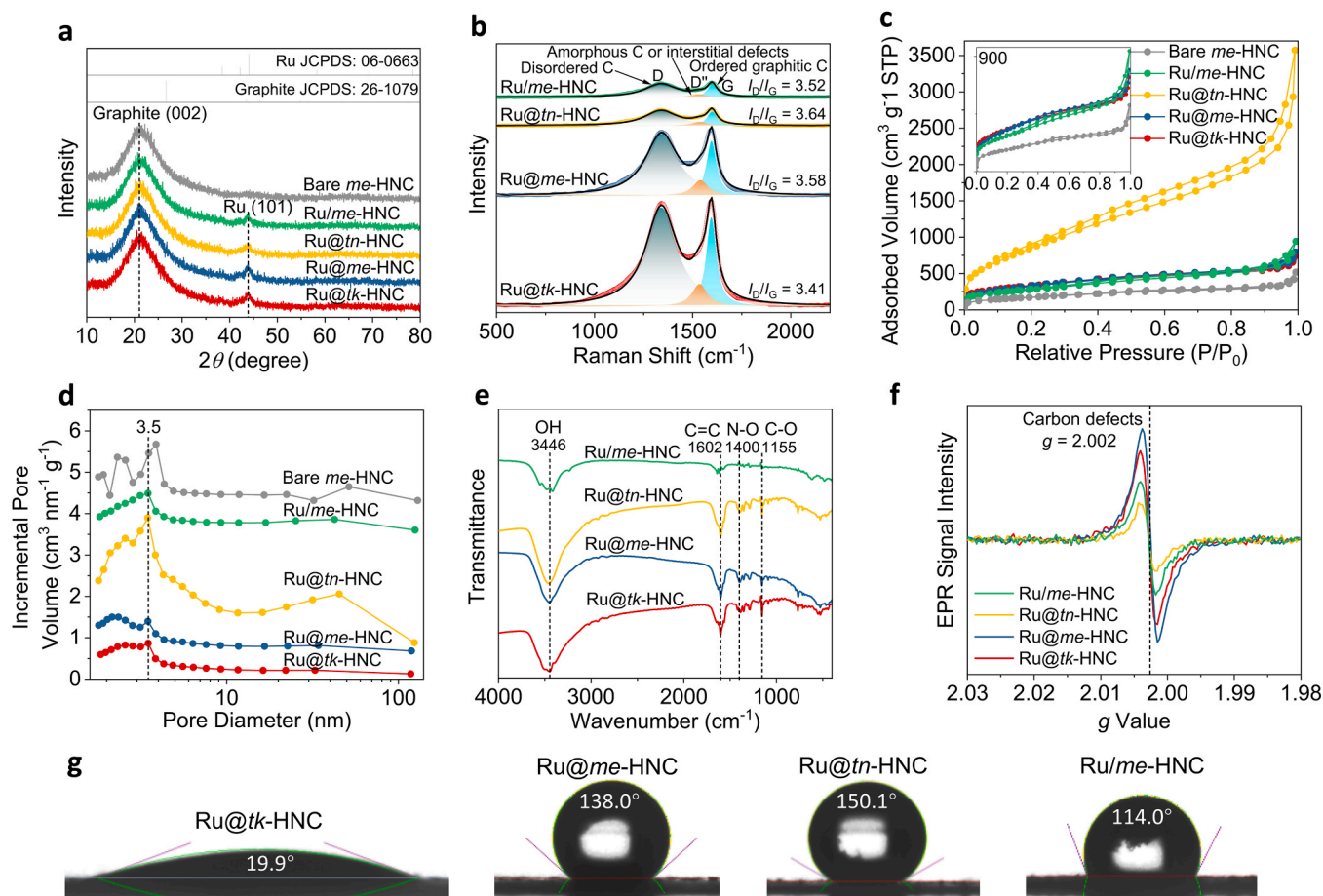
Fig. 2. (a) Power XRD patterns, (b) Raman spectra, (c) N_2 physisorption isotherms and the corresponding enlarged isotherms, (d) BJH pore size distributions based on the desorption isotherms, (e) FTIR spectra, (f) EPR spectra, and (g) water contact angles of the as-synthesized Ru@*tk*-HNC, Ru@*me*-HNC, Ru@*tn*-HNC, Ru/*me*-HNC catalysts and bare *me*-HNC.

indicated by temperature-programmed reduction of H_2 (H_2-TPR) below [39], and less hindrance to potential RuO_2 coalescence during carbonization by a thinner shell [40].

Fourier transform infrared spectra (FTIR) of Ru@*tk*-HNC, Ru@*me*-HNC, Ru@*tn*-HNC, and Ru/*me*-HNC were collected to analyze surface functional groups. In Fig. 2e, the four catalysts display characteristic peaks corresponding to C−O stretching, N−O stretching, C═C stretching, and OH vibration at 1155, 1400, 1602, and 3446 cm^{-1}, respectively [41], confirming the existence of doped N and abundant surface hydroxyl group on the catalysts.

In Fig. 2f, Ru@*tk*-HNC, Ru@*me*-HNC, Ru@*tn*-HNC, and Ru/*me*-HNC exhibit a strong electron paramagnetic resonance (EPR) response, likely induced by the defective sites of the carbon shells. In Fig. 2g, Ru@*tk*-HNC exhibits a lower water contact angle, while the water contact angles of Ru@*me*-HNC and Ru@*tn*-HNC are higher and comparable. This variation in hydrophobicity likely originates from differences in the content of surface polar functional groups. FTIR analysis has revealed the presence of OH group on the catalysts. As quantified by X-ray photoelectron spectroscopic (XPS) spectra below (Table S2), the surface OH/C ratio of Ru@*tk*-HNC is 0.01, which is twice that of Ru@*me*-HNC and Ru@*tn*-HNC (0.005), consistent with the variation in water contact angles. The comparative Ru/*me*-HNC catalyst, which exhibits a lower water contact angle than Ru@*me*-HNC, possesses a higher surface OH/C ratio of 0.02, reinforcing this argument.

3.2. Morphology and microstructure of yolk-shell Ru@HNC and supported Ru/me-HNC

On the basis of scanning electron microscopy (SEM), Ru@*tk*-HNC (Fig. 3a1 and Fig. S1a), Ru@*me*-HNC (Fig. 3b1 and Fig. S1b), and Ru@*tn*-HNC (Fig. 3c1 and Fig. S1c) exhibit a monodispersed and uniformly spherical morphology with a slightly rough surface. Notably, the transparency of these nanospheres gradually increases, particularly evident for Ru@*tn*-HNC (Fig. 3c1), indicating the development of hollow nanostructures and the progressive thinning of their shells. This thinning is further evidenced by a decrease in the average nanosphere diameter from 515 nm for Ru@*tk*-HNC to 427 nm for Ru@*me*-HNC, and then to 413 nm for Ru@*tn*-HNC. Additionally, Fig. S2 confirms that the hollow nanosphere morphologies of the final catalysts inherit from the template of SiO_2 nanospheres, with each fabrication step effectively preserving these nanosphere morphologies. Omitting the RuO_2 deposition and reduction steps yielded bare *me*-HNC nanospheres (Fig. S1d), and the subsequent deposition of Ru NPs maintains the hollow nanosphere morphology, albeit with slight increases in size and surface roughness (Fig. 3d1).

Transmission electron microscopy (TEM) provides a more detailed micro-level investigation. In Fig. 3a2−c2 and Fig. S3a−c, well-defined hollow yolk-shell nanospheres featuring darker carbon shells and small internally-encapsulated Ru NPs are evident. The element composition is confirmed through energy-dispersive X-ray (EDX) analysis (Fig. S4). Selected-area electron diffraction (SAED) images (insets in Fig. 3a2−c2) reveal diffraction rings corresponding to (101) and (113) planes of graphite carbon. Additionally, extra diffraction dots appear on
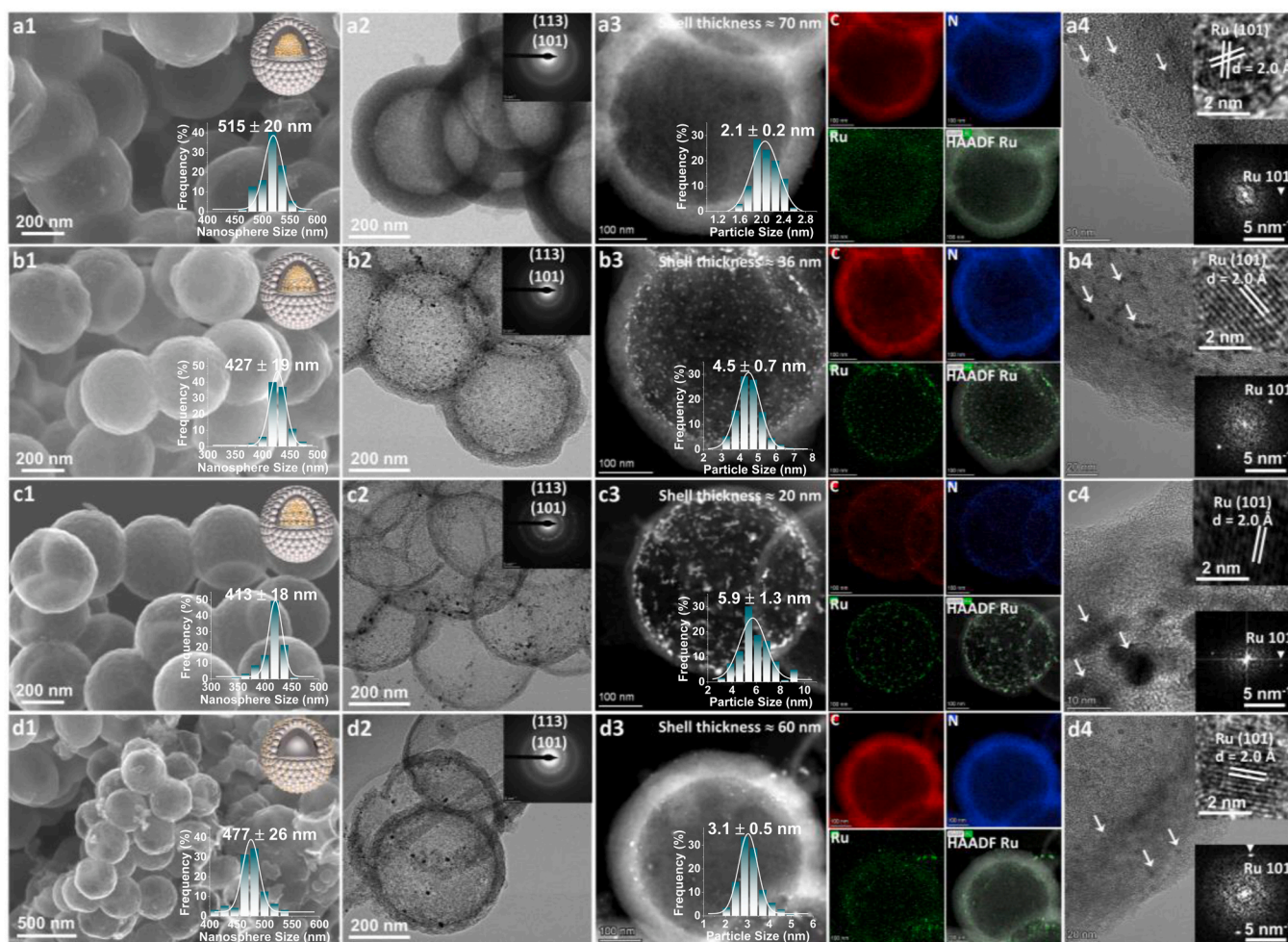
Fig. 3. (a1–d1) SEM images with schematic models and hollow nanosphere size distribution histograms, (a2–d2) TEM images with SAED patterns, (a3–d3) HAADF-STEM images with Ru particle size distribution histograms and corresponding mapping EDX images of C, N, Ru, and Ru HAADF-STEM images, and (a4–d4) magnified TEM images with HRTEM images and corresponding FFT patterns of the as-synthesized (a1–a4) Ru@*tk*-HNC, (b1–b4) Ru@*me*-HNC, (c1–c4) Ru@*tn*-HNC, and (d1–d4) Ru/*me*-HNC catalysts.

Ru@*me*-HNC and Ru@*tn*-HNC (insets in Fig. 3b2–c2), originating from crystallized Ru NPs, absent on Ru@*tk*-HNC (inset in Fig. 3a2), indicating its smaller Ru size. The shell thickness apparently decreases for Ru@*tk*-HNC, Ru@*me*-HNC, and Ru@*tn*-HNC, as quantitatively verified by high angle annular dark field imaging in scanning transmission electron microscopy (HAADF-STEM) images (Fig. 3a3–c3), measuring approximately 70, 36, and 20 nm for Ru@*tk*-HNC, Ru@*me*-HNC, and Ru@*tn*-HNC, respectively. Furthermore, HAADF-STEM images (Fig. 3a3–c3) and magnified TEM images (Fig. 3a4–c4 and Fig. S5a–c) prove the encapsulation of Ru NPs inside carbon shells. The Ru NPs gradually becomes larger with decreasing shell thickness, measuring 2.1, 4.5, and 5.9 nm for Ru@*tk*-HNC, Ru@*me*-HNC, and Ru@*tn*-HNC, respectively (insets in Fig. 3a3–c3). These small sizes demonstrate the efficient prevention of Ru agglomeration during carbonization and reduction at high temperatures by the shells, potentially ensuring resistance against Ru NP agglomeration during catalytic operations and thereby ensuring stability. In Fig. 3a4 for Ru@*tk*-HNC, it is illustrated that certain Ru NPs are anchored on the carbon shell, likely due to the easy access of small-sized Ru NPs into the pores of the carbon shell.

When depositing Ru NPs onto bare *me*-HNC, Fig. 3d2 and Fig. S3d evidence the retention of the hollow sphere morphology of bare *me*-HNC, highlighting its robust mechanical strength. Unlike the encapsulation of Ru NPs inside carbon shells observed on Ru@*tk*-HNC, Ru@*me*-HNC, and Ru@*tn*-HNC, the HAADF-STEM image (Fig. 3d3) and magnified TEM images (Fig. 3d4 and Fig. S5d) of Ru/*me*-HNC reveal the

distribution of Ru NPs on the outer surface of *me*-HNC. The mean size of Ru on Ru/*me*-HNC (3.1 nm) is slightly smaller than that on Ru@*me*-HNC, and the SAED pattern of Ru/*me*-HNC (inset in Fig. 3d2) closely resembles that of Ru@*me*-HNC.

To validate the distribution of each element, mapping EDX images are presented in Fig. 3a3–d3. N and C are uniformly distributed on all the catalysts, consistent with the presence of N—O group observed on the FTIR spectra. Ru mapping images and Ru HAADF-STEM images reveal the distribution of Ru both inside and on the carbon shell of Ru@*tk*-HNC, while for Ru@*me*-HNC and Ru@*tn*-HNC, Ru is confined inside the carbon shells. For Ru/*me*-HNC, Ru predominantly resides on the outer surface. These observations are further corroborated by overlapped mapping EDX images of C and Ru (Fig. S6). Besides, Si residues are evident throughout the entire hollow spheres for all catalysts (Fig. S7), potentially aiding in preventing the agglomeration of encapsulated Ru NPs and contributing to the effective dispersion of Ru.

The high-resolution TEM (HRTEM) images of Ru@*tk*-HNC, Ru@*me*-HNC, Ru@*tn*-HNC, and Ru/*me*-HNC are depicted in insets of Fig. 3a4–d4. Nearly spherical Ru NPs are observed on Ru@*tk*-HNC, Ru@*me*-HNC, and Ru@*tn*-HNC. Perfect lattice fringes are discernible on Ru. Their spacing of 2.0 Å, together with the corresponding fast Fourier transform (FFT) images, ensure the assignment of *hcp* Ru (101) plane. No lattice fringes and diffractions are visible on the carbon shells.

3.3. Chemical states and electronic metal–support interactions of yolk-shell Ru@HNC and supported Ru/me-HNC

The influences of carbon shell thickness and Ru location on chemical states and electronic metal–support interactions (EMSI) were probed using XPS spectra. The survey spectra in Fig. S8a confirm the existence of Ru, C, N, and O elements on Ru@*tk*-HNC, Ru@*me*-HNC, Ru@*tn*-HNC, and Ru/*me*-HNC. The invisibility of Si in Fig. S8a may be attributed to its low content, as indicated by the Si 2*p* spectra in Fig. S8b, which exhibit a peak at a binding energy (BE) of 102.5 eV attributable to SiO_2 [42], consistent with the mapping EDX results. No signal is detected on the Br 3*d* spectra (Fig. S8c), revealing the complete removal of CTAB during the synthesis process.

On the Ru 3*p* spectra (Fig. 4a), two peaks within the BE ranges of 461.6−462.3 eV ($3p_{3/2}$) and 483.8−484.5 eV ($3p_{1/2}$) are discerned for each catalyst, with a consistent $3p_{1/2}$−$3p_{3/2}$ BE separation of 22.2 eV (Table S3), ascertaining the assignment of metallic Ru (Ru^0) [42]. The significantly stronger peak intensity of Ru/*me*-HNC compared to the others demonstrates the location of Ru on the outer carbon shell surface for Ru/*me*-HNC, whereas Ru is encapsulated inside the carbon shells for Ru@*tk*-HNC, Ru@*me*-HNC, and Ru@*tn*-HNC. Conspicuously, a negative BE shift of Ru 3*p* peaks in the sequence of Ru/*me*-HNC (462.3 eV) > Ru@*tk*-HNC (462.2 eV) > Ru@*me*-HNC (461.9 eV) > Ru@*tn*-HNC (461.6 eV) is recognized, revealing the existence of EMSI and electron transfer from the outer shell to Ru^0 on yolk-shell Ru@HNC. The degree of electron richness increases with decreasing carbon shell thickness. Furthermore, a 0.4 eV lower BE of Ru^0 on Ru@*me*-HNC compared to Ru/*me*-HNC confirms the induction of EMSI by the unique yolk-shell structure.

To elucidate the origin of EMSI, the N 1*s* spectra are analyzed. In Fig. 4b, two types of N 1*s* peaks at BE of 398.3 eV attributable to pyridinic-N and 401.1 eV assigning to graphitic-N are disclosed (Table S4) [43]. The existence of N dopants is further confirmed by the O−N signal on the O 1*s* spectra (Fig. 4c and Table S2) [5]. The surface N/C ratios are essentially identical on Ru@*tk*-HNC, Ru@*me*-HNC, Ru@*tn*-HNC, and Ru/*me*-HNC (Table S4), which is reasonable given that the nitrogen on the catalysts originates from the APTES modifier, and the APTES content is identical for synthesizing each catalyst. Moreover, the surface pyridinic-N/Ru^0 and graphitic-N/Ru^0 molar ratios were calculated (Table S3). Interestingly, the surface pyridinic-N/Ru^0 values exhibit an increased trend: Ru/*me*-HNC (0.30) < Ru@*tk*-HNC (0.32) < Ru@*me*-HNC (0.42) < Ru@*tn*-HNC (0.50), consistent with the increasing order of electron-rich degree of Ru on these catalysts. The potentially higher accessibility of pyridinic-N and fewer surface atoms of encapsulated Ru on the yolk-shell catalyst with a higher surface area such as thinner-shelled Ru@HNC may contribute to this trend [44]. However, the graphitic-N/Ru^0 and total N/Ru^0 values do not follow this trend, suggesting that pyridinic-N species in the carbon shells may be the pivotal contributing factor to EMSI on the yolk-shell Ru@HNC catalysts.

To ascertain the decisive role of pyridinic-N in EMSI, the C 1*s* and Ru 3*d* spectra are analyzed. In Fig. 4d−f, Fig. S8d and Table S5, the C 1*s* spectra of Ru@*tk*-HNC, Ru@*me*-HNC, Ru@*tn*-HNC, and Ru/*me*-HNC reveal four types of carbon species: graphite C [42], C−OH [14], C=N [45], and OH−C=O [14]. The presence of OH−C=O species aligns with the deconvolution of the O=C peak on the O 1*s* spectra (Fig. 4c). The BEs of graphite C, C−OH, and OH−C=O remain consistent regardless of carbon shell thickness and Ru location, while a positive BE shift of the pyridinic-N-associated C=N species is discerned in the sequence of Ru/*me*-HNC (287.0 eV) < Ru@*tk*-HNC (287.2 eV) < Ru@*me*-HNC (287.4 eV) < Ru@*tn*-HNC (287.6 eV), revealing electron donation from C=N to Ru^0. This phenomenon can be rationalized by the lone-pair electrons of pyridinic-N, which exhibit a strong tendency to interact with the empty orbit of Ru^0 [45]. The deconvoluted Ru^0 $3d_{5/2}$ and $3d_{3/2}$ peaks in Fig. 4d−f and Fig. S8d further confirm the electronic interaction between pyridinic-N and Ru^0. Additionally, in Table S6, the surface Ru/C molar ratio of Ru/*me*-HNC is approximately ten times those of Ru@*tk*-HNC, Ru@*me*-HNC, and Ru@*tn*-HNC, all of which are lower than the corresponding bulk Ru/C molar ratios, indicating the encapsulation
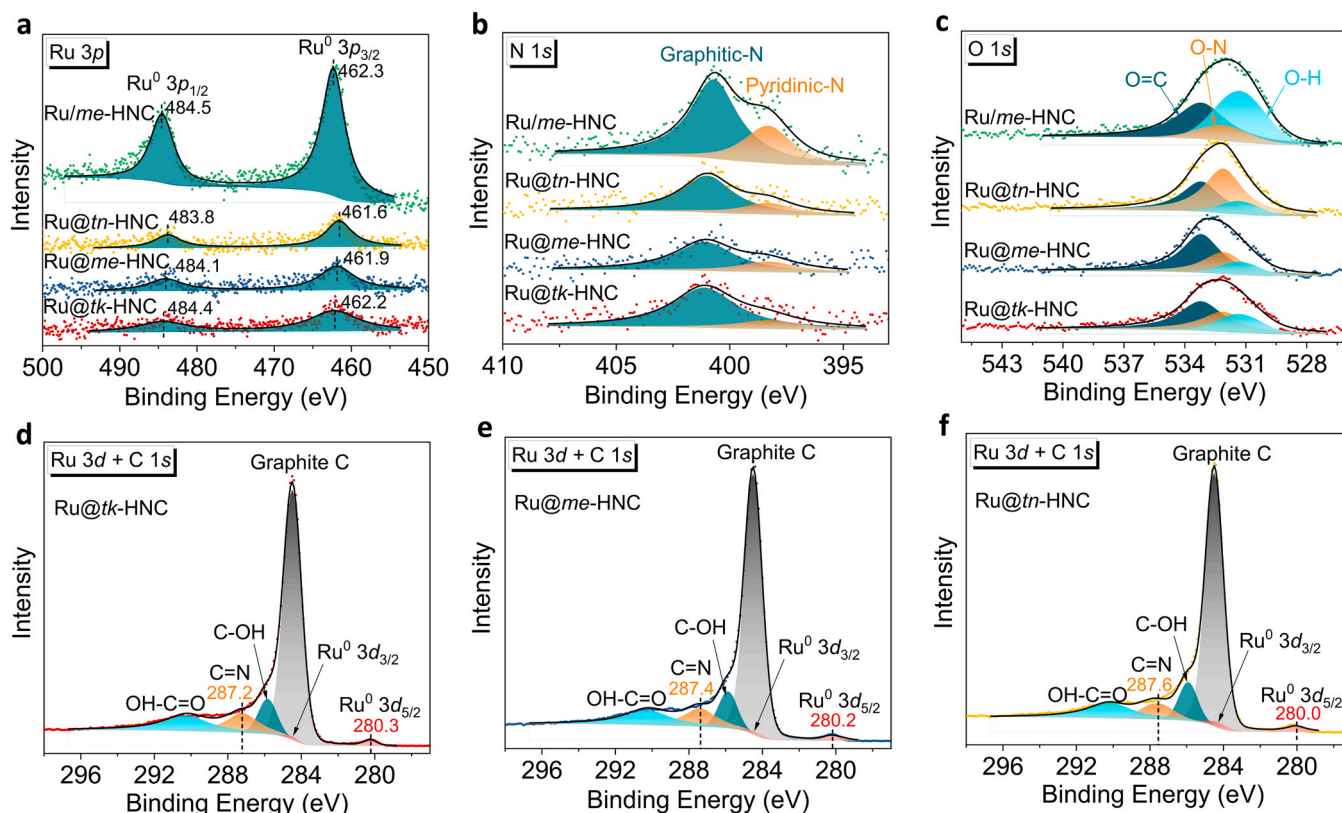

Fig. 4. (a) Ru 3*p*, (b) N 1*s*, (c) O 1*s*, and (d−f) Ru 3*d* and C 1*s* XPS spectra of the as-synthesized Ru@*tk*-HNC, Ru@*me*-HNC, Ru@*tn*-HNC, and Ru/*me*-HNC catalysts.

of Ru inside carbon shells for Ru@*tk*-HNC, Ru@*me*-HNC, and Ru@*tn*-HNC.

To further confirm the pivotal role of N dopant in enhancing EMSI, the Ru 3*d* spectrum of Ru/AC is displayed in Fig. S9. The surface Ru/C molar ratio on Ru/AC calculated from Fig. S9 is 0.06, which is six times that of Ru/*me*-HNC and approximately sixty times those of Ru@HNC (Table S6), despite having identical Ru loadings. This large difference indicates severe agglomeration of Ru on AC, and consequently, a much larger Ru size, rendering Ru a lower binding energy [46]. Nevertheless, the Ru^0 $3d_{5/2}$ BE of Ru/AC remains at 280.4 eV, higher than those observed on all the yolk-shell Ru@HNC catalysts. This observation evidences that AC, lacking N dopant, fails to transfer electrons to Ru and that the pyridinic-N species on the carbon shells of Ru@HNC are pivotal in enhancing EMSI. In summary, XPS analysis has demonstrated that the unique yolk-shell structure with encapsulated Ru NPs and thinning carbon shells of the Ru@HNC catalysts facilitate the exposure of more surface pyridinic-N species. This contributes to increased electron transfer from pyridinic-N to Ru^0, enhancing EMSI and rendering Ru^0 more electron-rich.

H_2-TPR is employed to validate the EMSI. In Fig. 5, two low-temperature peaks at 129/253 °C for Ru@*tk*-HNC, 186/265 °C for Ru@*me*-HNC, and 208/306 °C for Ru@*tn*-HNC are ascribed to the reduction of Ru^{4+} to Ru^{3+} and Ru^{3+} to Ru^0, respectively [47]. Peaks observed over 400 °C are likely due to the partial gasification of carbon to methane and/or the decomposition of the oxygen-containing surface groups on carbon [47,48]. The reduction temperatures of Ru species increase with the thinning of the carbon shell, indicating a stronger interaction, which aligns with the previous observation that unsaturated N groups on carbon facilitate the anchoring of Ru [49]. Upon depositing Ru on the outer surface of *me*-HNC, the reduction temperatures of Ru species of unreduced Ru/*me*-HNC occur at 156 °C and 216 °C, both lower than the unreduced Ru@*me*-HNC counterparts, affirming an enhanced interaction through the formation of a yolk-shell structure. Furthermore, the hydrogen consumption of Ru/*me*-HNC obviously exceeds those of Ru@HNC, which can be attributed to the higher degree of methanation due to the deposition of Ru on the outer surface of *me*-HNC.

3.4. Acid-base characteristics of yolk-shell Ru@HNC and supported Ru/me-HNC

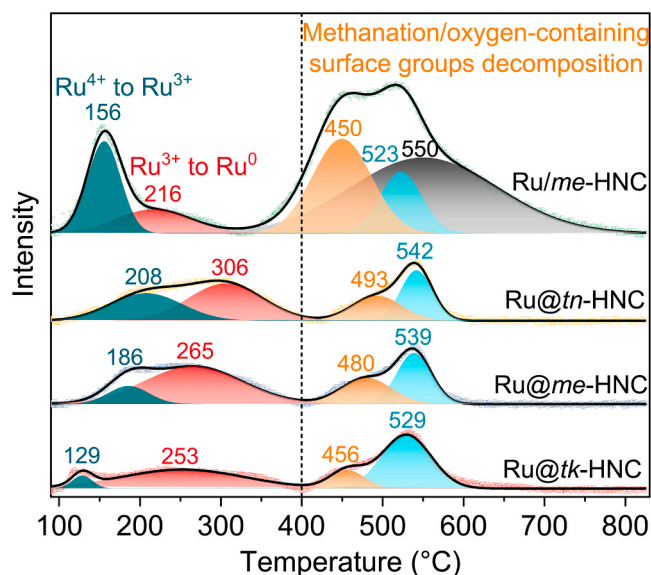In Fig. 6A, the temperature-programmed desorption of CO_2 (CO_2-

Fig. 5. H_2-TPR profiles of the unreduced Ru@*tk*-HNC, Ru@*me*-HNC, Ru@*tn*-HNC, and Ru/*me*-HNC catalysts.

TPD) profiles of Ru@*tk*-HNC, Ru@*me*-HNC, and Ru@*tn*-HNC all exhibit two peaks below 400 °C (representing weak basic sites) and two peaks above 500 °C (indicative of strong basic sites) [50]. With the thinning of the carbon shell, the strength of weak basic sites at around 330 °C basically remains unchanged, while that below 300 °C intensifies, and the strengths of two strong basic sites diminish. In contrast, for Ru/*me*-HNC, an additional peak at 437 °C attributable to moderate basic sites emerges [50], and the strengths of the strong basic sites surpass those of Ru@*me*-HNC. According to the corresponding integral intensities, the quantities of weak, moderate, and strong basic sites, as well as the total basic amounts, were estimated (Fig. 6B). Apparently, variations in shell thickness induce minimal changes in the total basic amount, while encapsulating Ru inside carbon shell (Ru@*me*-HNC) results in approximately one-quarter of the total basic amount observed on the corresponding supported Ru/*me*-HNC catalyst.

In Fig. 6C, the NH_3-TPD profile of Ru@*tk*-HNC exhibits two peaks at 198 °C (indicative of weak acid sites) and 336 °C (representing moderate acid sites) [51]. For Ru@*me*-HNC, Ru@*tn*-HNC, and Ru/*me*-HNC, in addition to the weak and moderate acid sites, an additional peak attributed to strong acid sites emerges [51]. The corresponding acid amounts resulted from peak intensities are depicted in Fig. 6D, demonstrating that decreasing the carbon shell thickness of yolk-shell Ru@HNC contributes to an increment in the total acid amount, and encapsulating Ru inside *me*-HNC (Ru@*me*-HNC) leads to slightly fewer acid sites compared to depositing Ru on *me*-HNC (Ru/*me*-HNC).

Fig. 6E presents the FTIR spectra of pyridine (Py-IR). Ru@*tk*-HNC, Ru@*me*-HNC, Ru@*tn*-HNC, and Ru/*me*-HNC exhibit both Lewis acid sites-coordinated Py (L-Py, 1446 cm^{-1}) and Brønsted acid sites-bonded Py (PyH$^+$, 1543 cm^{-1}), along with faintly physisorbed Py (ph-Py, 1576 cm^{-1}) and hydrogen-bonded Py (hb-Py, 1595 cm^{-1}), as well as strong L-Py (1607 or 1620 cm^{-1}) and strong PyH$^+$ (1640 cm^{-1}) [41]. The ph-Py and hb-Py bands are scarcely visible at 150 °C, ensuring accurate calculations of Lewis and Brønsted acid amounts at this temperature. As illustrated in Fig. 6F, Lewis acid sites predominate, and their quantities, along with the summation of these two types of acid sites, increase with the thinning of the carbon shell. Also, Py-IR confirms that Ru@*me*-HNC exhibits lower acidity than Ru/*me*-HNC.

3.5. Catalytic behaviors of yolk-shell Ru@HNC and supported Ru/me-HNC

The catalytic behaviors of Ru@*tk*-HNC, Ru@*me*-HNC, Ru@*tn*-HNC, and Ru/*me*-HNC in selective hydrogenation of LA were tested at 30 °C and 1.0 MPa, employing H_2O as the reaction solvent. The time-dependent reaction profiles are depicted in Fig. 7a, illustrating a steady decrease in LA content. Throughout the entire reaction period for each catalyst, only GVL was detected as a product, maintaining a selectivity of 99.9% towards GVL. Fitting the residual LA content against reaction time yields exponential declines (Fig. S10), resulting in nearly complete consumption within 3.5 h on each catalyst. However, the consumption rates vary with carbon shell thickness and Ru location, with the Ru@*me*-HNC catalyst exhibiting a higher consumption rate than Ru@*tk*-HNC and Ru@*tn*-HNC. This trend is quantitatively supported by the initial weight-specific activity (r_0) (Table 1). Moreover, encapsulating Ru inside carbon shell (Ru@*me*-HNC) also enhances the consumption rate and r_0 compared to supporting Ru on hollow carbon spheres (Ru/*me*-HNC), underscoring the superiority of the yolk-shell structure in enhancing the activity. The variation of r_0 may be jointly determined by both the number and nature of surface Ru sites. Enhancing electron density of metal NPs has been identified to facilitate their catalytic activity in LA hydrogenation [38]. As exhibited in Fig. S11, despite Ru@*tn*-HNC being the most electron-rich, its obviously lower number of surface Ru sites in each catalytic run ($N_{surface}$, Table S1) likely contributes to the lowest r_0. Conversely, for Ru/*me*-HNC, Ru@*tk*-HNC, and Ru@*me*-HNC, their higher and similar $N_{surface}$, coupled with gradually enhanced electron-rich Ru, may result in an increase in
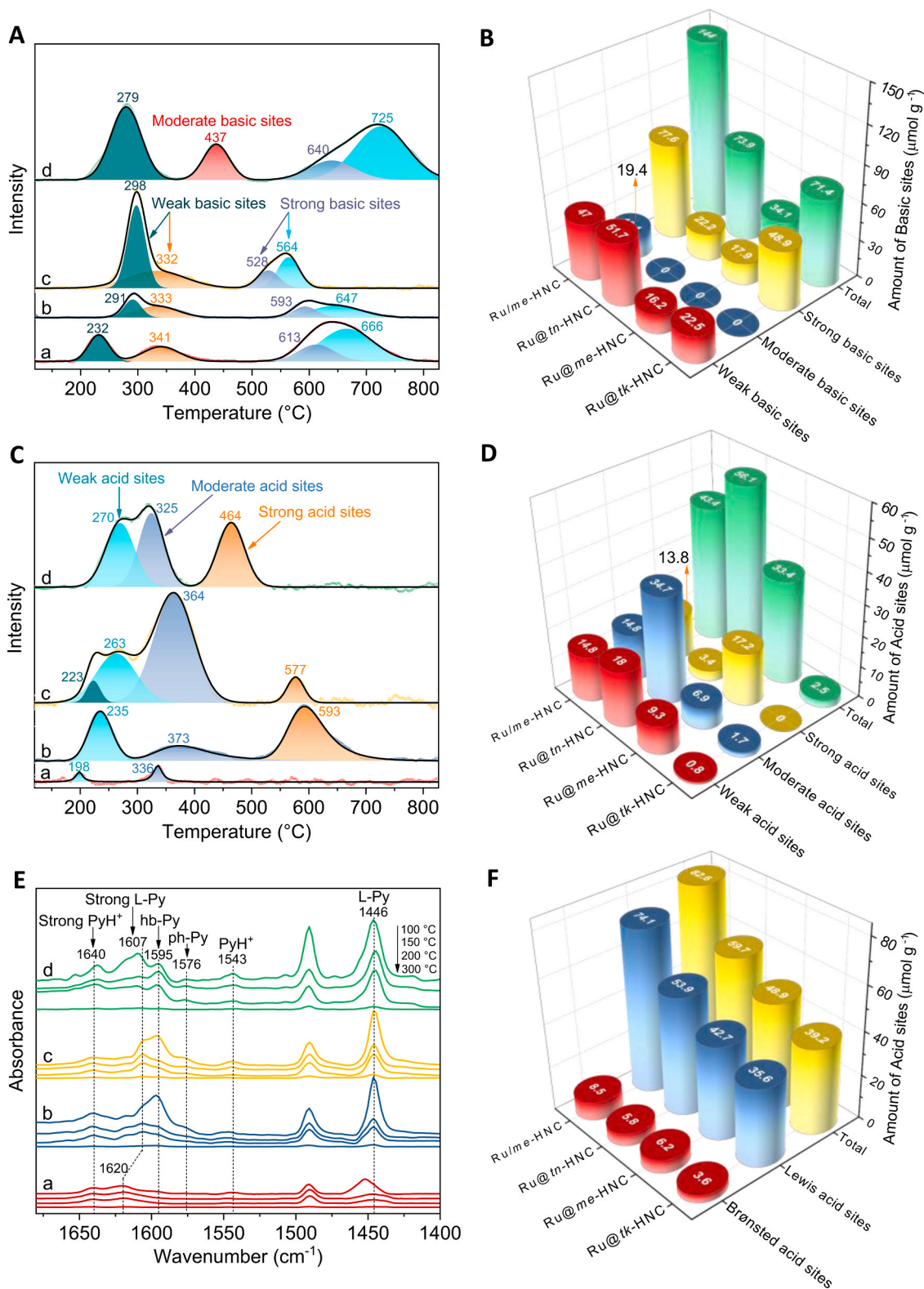
Fig. 6. (A) CO_2-TPD profiles, (B) the amounts of basic sites derived from CO_2-TPD, (C) NH_3-TPD profiles, (D) the amounts of acid sites derived from NH_3-TPD, (E) Py-IR spectra collected at 100 °C, 150 °C, 200 °C, and 300 °C, and (F) the amounts of acid sites based on Py-IR spectra of the as-synthesized (a) Ru@*tk*-HNC, (b) Ru@*me*-HNC, (c) Ru@*tn*-HNC, and (d) Ru/*me*-HNC catalysts. The values in figure (F) are based on the Py-IR spectra collected at 150 °C.

r_0. All three yolk-shell Ru@HNC catalysts and the supported Ru/*me*-HNC catalyst exhibit higher consumption rates than Ru/AC, highlighting the advantage of hollow carbon spheres as a support material.

For further comparison of intrinsic activities, the TOFs of LA were

calculated (Table 1). The higher TOF observed on Ru@*me*-HNC compared to Ru/*me*-HNC provides evidence that the yolk-shell structure can intrinsically enhance the activity of Ru. A gradual increment from 8283.3 to 18733.4 h^{-1} with the thinning of the carbon shell of Ru@*tk*-HNC, Ru@*me*-HNC, Ru@*tn*-HNC underscores the pivotal role of shell
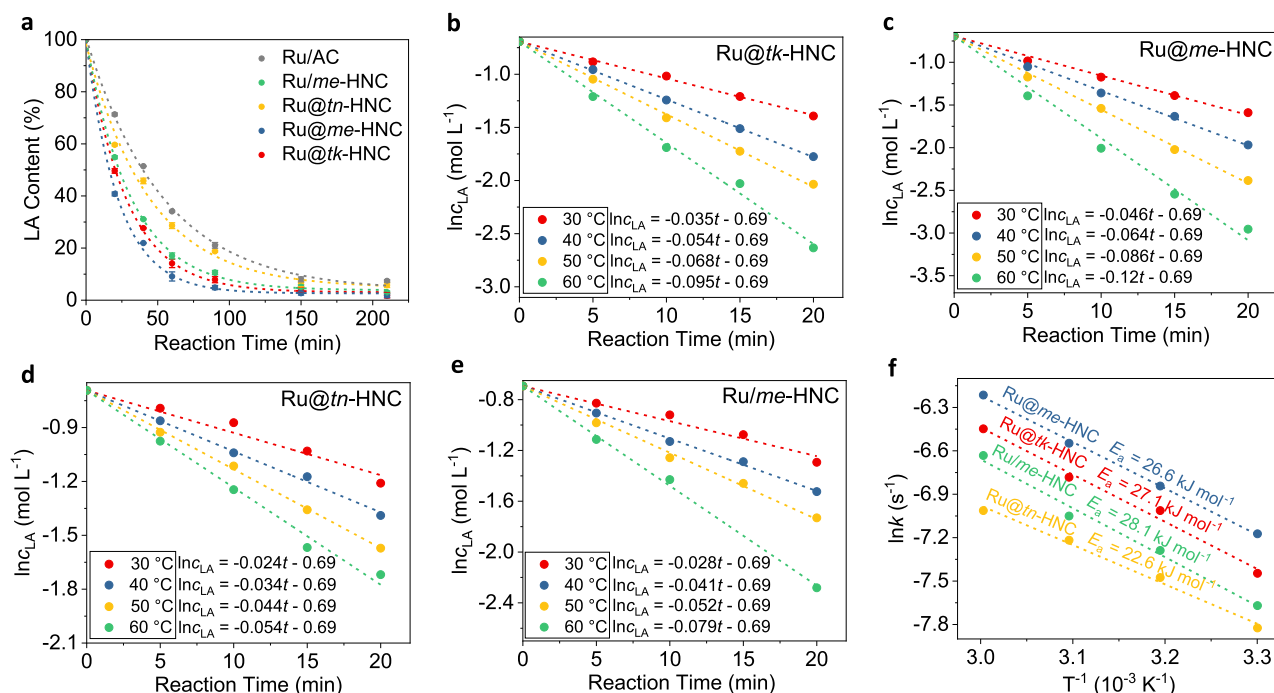
Fig. 7. (a) The courses of LA hydrogenation over the as-synthesized Ru@*tk*-HNC, Ru@*me*-HNC, Ru@*tn*-HNC, Ru/*me*-HNC, and Ru/AC catalysts. Reaction conditions: 56 μmol of Ru (catalyst mass: 60.1, 58.8, 57.8, 58.8, and 58.8 mg for Ru@*tk*-HNC, Ru@*me*-HNC, Ru@*tn*-HNC, Ru/*me*-HNC, and Ru/AC, respectively), 10 mmol of LA, 20 mL of H_2O, temperature of 30 °C, H_2 pressure of 1.0 MPa, and stirring rate of 1600 rpm. The catalytic performances were assessed in duplicate, and the results from replicate runs agree to within ± 2%; (b–e) The plots of the natural logarithm of LA concentration with respect to reaction time under 30 °C, 40 °C, 50 °C, and 60 °C over the as-synthesized Ru@*tk*-HNC, Ru@*me*-HNC, Ru@*tn*-HNC, and Ru/*me*-HNC catalysts; (f) The corresponding Arrhenius plots for the reaction rate constants.

Table 1
Results of LA hydrogenation over yolk-shell Ru@hollow pyridinic-N-doped carbon nanospheres with thick, moderate, and thin shell thicknesses, and externally supported Ru/*me*-HNC and Ru/AC catalysts.[a].

Entry	Catalyst	t (h)	Conversion (%)	GVL Selectivity (%)	Yield (%)	r_0[b]	TOF (h^{-1})
1	Ru@*tk*-HNC	3.5	98.2	99.9	98.1	5.66	8283.3
2	Ru@*me*-HNC	3.5	98.3	99.9	98.2	7.31	11808.5
3	Ru@*tn*-HNC	3.5	94.3	99.9	94.2	3.63	18733.4
4	Ru/*me*-HNC	3.5	97.0	99.9	96.9	5.27	7378.0
5	Ru/AC	3.5	92.6	99.9	92.5	3.06	6647.6
6[c]	Ru@*me*-HNC	3.5	70.0	99.9	69.9	n.c.[g]	n.c.
7[d]	Ru@*me*-HNC	3.5	78.0	99.9	77.9	n.c.	n.c.
8[e]	Ru@*me*-HNC	3.5	95.0	99.9	94.9	n.c.	n.c.
9[f]	Ru@*me*-HNC	3.5	73.0	99.9	72.9	n.c.	n.c.

[a] Reaction conditions: 56 μmol of Ru (catalyst mass: 60.1, 58.8, 57.8, 58.8, and 58.8 mg for Ru@*tk*-HNC, Ru@*me*-HNC, Ru@*tn*-HNC, Ru/*me*-HNC, and Ru/AC, respectively), 10 mmol of LA, 20 mL of H_2O, temperature of 30 °C, H_2 pressure of 1.0 MPa, and stirring rate of 1600 rpm.
[b] Initial weight-specific activity, unit in $mmol_{LA}\ g_{cat}^{-1}\ min^{-1}$.
[c] The solvent of H_2O was replaced to methanol.
[d] The solvent of H_2O was replaced to ethanol.
[e] The solvent of H_2O was replaced to cyclohexane.
[f] The solvent of H_2O was replaced to anisole.
[g] n.c.: not calculated.

thickness in determining the intrinsic activity. Furthermore, the highest TOF achieved with Ru@*tn*-HNC is 2.5 times that of Ru/AC. A detailed comparison between Ru@*tn*-HNC and recently reported Ru-based catalysts is summarized in Table S7. Despite having a lower TOF compared to catalysts such as 3D oxide-derived Ru (59400 h^{-1}) [25] and $Ru_{0.18}/Al_2O_3$/NC (26400 h^{-1}) [52], Ru@*tn*-HNC exhibits a certain degree of improvement over numerous catalysts, for example, Ru/nanodiamonds-900 (about 6000 h^{-1}) [24], Ru_1Co@NC-1.1 (3500 h^{-1}) [53], Ru/N-doped carbon nanospheres (1127 h^{-1}) [54], Ru_1@WO_x/CN (1060 h^{-1}) [55], Ru/mesoporous carbon (12024 h^{-1}) [56], and $Ru_{0.7}Ni_{0.3}$−ordered mesoporous carbon (2936 h^{-1}) [57]. The kinetics results are presented in Fig. 7b−f. When

correlating lnc_{LA} (c_{LA} = LA concentration) with reaction time (t) at temperatures ranging from 30 to 60 °C, excellently linear relationships are observed on both yolk-shell and supported Ru catalysts, revealing a first-order reaction with respect to LA. The corresponding rate constants (k) at each temperature were calculated using $lnc_{LA} = -kt + lnc_{LA,0}$. Subsequently, Arrhenius plots of $lnk = lnk_0 - E_a/RT$ are generated to determine the apparent activation energy (E_a, Fig. 7f). The resulting E_a for Ru/*me*-HNC, Ru@*tk*-HNC, Ru@*me*-HNC, and Ru@*tn*-HNC are 28.1, 27.1, 26.6, and 22.6 kJ mol^{-1}, respectively, in accordance with the enhancement of TOFs.

Table 1 (entries 6−9) further indicates that replacing water, the reaction solvent, with other organics such as methanol, ethanol, cyclohexane, and anisole does not affect the selectivity towards GVL, while

the LA conversion decreases. This observation highlights the superiority of water as a reaction solvent. Differences in polarity, hydrogen solubility, and kinetic diameter of these solvents may jointly influence the LA conversion [58,59]. Among these, water, possessing the highest polarity, can reduce the free energy of activation for all elementary reactions in LA hydrogenation [58] and participate in the hydrogenation of the C=O group of LA [59], thus enhancing catalytic activity. Fig. S12 elucidates that the rate of LA consumption could be boosted by increasing temperature and pressure, but it will be suppressed by elevating the initial LA concentration.

3.6. Catalytic mechanism

Prior to discussing the catalytic mechanism, possible mass transfer effects are assessed using the Weisz-Prater criterion [60]. The calculation details are outlined in the Supplementary Material. The values of the Weisz-Prater criterion for LA and H_2 on all the catalysts are much lower than the threshold to neglect mass transfer limitation, implying that the reactions are governed by a kinetic regime.

Although GVL can be generated via two distinct hydrogenation pathways (Scheme S1), it has been established that at reaction temperatures below 150 °C on Ru/C, GVL exclusively forms via the intramolecular esterification of the intermediate 4-hydroxypentanoic acid
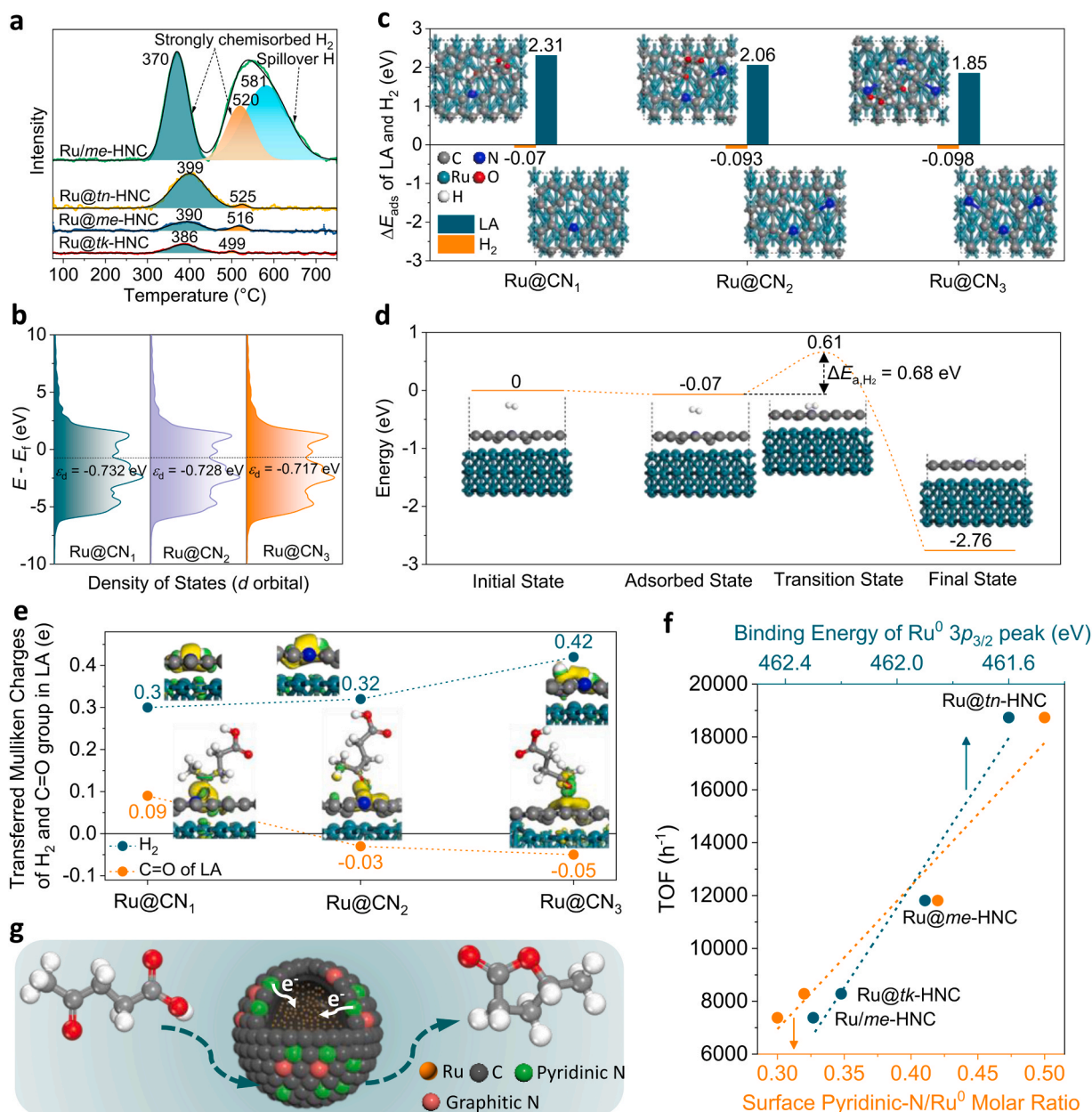

Fig. 8. (a) H_2-TPD profiles of the as-synthesized Ru@*tk*-HNC, Ru@*me*-HNC, Ru@*tn*-HNC, and Ru/*me*-HNC catalysts; (b) Electronic density of states of *d* orbital and calculated *d*-band center of Ru@CN heterostructure slab surface models with increased pyridinic-N atom numbers; (c) Calculated adsorption energy of LA and H_2 on Ru@CN models and corresponding top views of adsorption configurations after geometric optimization; (d) Calculated adsorption and dissociation paths of H_2 on Ru@CN_1 model and corresponding side views of optimized configurations; (e) Transferred Mulliken charges of H_2 and C=O group in LA after adsorbing and dissociating (for LA, only adsorbing) on Ru@CN models and corresponding side views of differential charge density after geometric optimization. Isosurface: ± 0.03 e $Å^{-3}$ for H_2 and ± 0.004 e $Å^{-3}$ for LA. Green and yellow regions represent electron accumulation and depletion, respectively; (f) Correlations of TOFs of LA~surface pyridinic-N/Ru^0 molar ratios and TOFs of LA~binding energies of Ru^0 $3p_{3/2}$ peak of the as-synthesized Ru@*tk*-HNC, Ru@*me*-HNC, Ru@*tn*-HNC, and Ru/*me*-HNC catalysts; (g) Manipulating mechanism of pyridinic-N on carbon shell on the catalytic performances of encapsulated Ru NPs in selective hydrogenation of LA to GVL.

(HPA) [61]. Moreover, the existence of more Lewis acid sites facilitates this intramolecular esterification process, as the conversion of HPA may be initiated by these sites, thereby promoting higher activity [27]. Consequently, the progressive increase in the quantity of Lewis acid sites achieved by thinning the carbon shell of Ru@*tk*-HNC, Ru@*me*-HNC, and Ru@*tn*-HNC could account for their augmented TOFs. However, despite the Ru*me*-HNC catalyst possessing a higher quantity of Lewis acid sites than Ru@*me*-HNC, it still demonstrates a lower TOF, implying that Lewis acid sites alone do not entirely determine the catalytic performances.

Selective hydrogenation of LA is a structure-sensitive reaction [62], necessitating consideration of Ru particle size to discern differences in TOFs. At the first sight, it was unexpected that the effect of Ru size on activity demonstrated in this work diverges from previous ones [62,63]. Namely, the TOF of LA is lower on Ru@HNC with a smaller Ru size, whereas it is higher on Ru/C with a smaller Ru size in the range of 1.2–2.9 nm [63], and it varies volcanically with Ru size in the range of 1−3 nm on Ru/C and Ru/Al$_2$O$_3$, peaking at approximately 1.5 nm [62]. This contradiction may arise from that the yolk-shell Ru@HNC catalyst with a smaller Ru size has a thicker carbon shell, which potentially covers more active sites available for LA hydrogenation, leading to a lower activity.

In addition to the geometrical feature of Ru, the electronic configuration of Ru is also pivotal to the intrinsic activity in LA hydrogenation, as it affects the adsorption of H$_2$ and LA molecules, as well as R−COOH breaking [41,53]. XPS has implied an enhancement in the electron-rich degree of Ru^0 by forming yolk-shell structure and thinning shell thickness. Consequently, H$_2$-TPD and DFT computations were conducted to study the H$_2$ and LA adsorption behaviors on Ru@*tk*-HNC, Ru@*me*-HNC, Ru@*tn*-HNC, and Ru*me*-HNC. As displayed in Fig. 8a, H$_2$ desorption primarily occurs in the temperature range of 386−399 °C, accompanied by a faint desorption ranging in 499−525 °C for the three yolk-shell catalysts, both attributing to strongly chemisorbed H$_2$. The presence of two desorption peaks may be attributed to H−H splitting. The desorption temperatures of chemisorbed H$_2$ increase as a result of promoting the electron-rich degree of Ru^0, manifesting an enhancement in the interaction between Ru^0 and H atoms. When supporting Ru NPs on *me*-HNC instead of encapsulating them inside the carbon shell, the main desorption peak of Ru*me*-HNC appears at 370 °C, which is 20 °C lower than that of Ru@*me*-HNC and also the lowest among the four catalysts. This lowest desorption temperature verifies the argument of electron-rich-Ru^0-induced enhancement in Ru^0−H interaction, since Ru*me*-HNC exhibits the lowest electron density. In addition, distinct from yolk-shell catalysts, Ru*me*-HNC gives an extra higher desorption peak at 581 °C, with hydrogen desorption continuing even above 600 °C, indicating hydrogen spillover from Ru to *me*-HNC [53]. In terms of peak intensities, Ru*me*-HNC demonstrates evidently higher integral intensity than the yolk-shell catalysts, resulting in more H species. However, despite this, the TOF of Ru*me*-HNC is the lowest, hinting that the stronger Ru^0−H interaction is more important than the quantity of H species for achieving high activity. For selective hydrogenation of LA, appropriate H$_2$ adsorption strength is crucial, as too weak adsorption fails to activate H$_2$, while too strong adsorption leads to difficult desorption [53]. Therefore, the suitably enhanced Ru^0−H interaction induced by improving the electron-rich degree of Ru^0 may be another critical factor responsible for the promoted TOFs.

The enhancement of reactant adsorption by increasing pyridinic-N on the carbon shell of the yolk-shell Ru@HNC catalysts is further examined by DFT calculations. Firstly, the crystal structures of ruthenium and carbon supercells were optimized. In Fig. S13, both bulk Ru and C exhibit a hexagonal crystal structure. The computed lattice parameters of Ru (Table S8) and C (Table S9) closely match the corresponding experiment values, with a deviation below 1.3% and 3.2%, respectively, meeting the reliability criteria of DFT [64]. Subsequently, to simulate the yolk-shell Ru@HNC catalysts with increased pyridinic-N in carbon shell, three heterostructure slab surface models were

constructed by covering a carbon layer with one to three pyridinic-N atoms on metallic Ru (Ru@CN$_1$, Ru@CN$_2$, Ru@CN$_3$, Fig. S14 and Table S10). Based on these optimized models, the band gap and electronic density of states (DOS) were calculated with the set path in the Brillouin zone (Table S11). As exhibited in Fig. S15, all models display a continuous total DOS near the Fermi level, indicating their metallic characteristic. According to the DOS of *d* orbitals, the *d*-band center (ε_d) was calculated (Fig. 8b). ε_d is regarded as a descriptor of the intrinsic catalytic activity of transition metals [65]. A higher ε_d indicates stronger bonding between adsorbate and active sites due to a reduction in antibonding orbital filling [65]. Therefore, the positively shifted ε_d of Ru@CN$_1$, Ru@CN$_2$, and Ru@CN$_3$ toward the Fermi level may suggest an enhancement of reactant adsorption on these models, which can be validated by the calculated adsorption energy (ΔE_{ads}) of LA and H$_2$ (Fig. 8c and Fig. S16a1−c1). In Fig. S16a1−c1, LA adopts a C=O group adsorption configuration, which is reasonable since C=O hydrogenation is the rate-determining step for the LA-to-GVL process [53]. The ΔE_{ads} of LA negatively shifts with the increment in pyridinic-N atom number, demonstrating that pyridinic-N facilitates C=O adsorption, thereby boosting its hydrogenation.

For H$_2$ (Fig. 8c and Fig. S16a2−c2), its ΔE_{ads} also exhibits a negative shift as the number of pyridinic-N atoms increases, revealing promoted adsorption. Aside from adsorption, the dissociation of H$_2$ into active H atoms is important in selective hydrogenation of LA. Therefore, the H$_2$ dissociation paths were calculated on the representative Ru@CN$_1$ model. As depicted in Fig. 8d and Fig. S17, H$_2$ undergoes an adsorption-transition state-dissociation process. The significantly lower energy of the final state (−2.76 eV) demonstrates that the dissociation of H$_2$ into two active H atoms on Ru@CN$_1$ is thermodynamically favored, necessitating the overcoming of a low energy barrier of 0.68 eV. Meanwhile, Mulliken population analysis (Fig. 8e and Fig. S18a1−c1) reveals that H$_2$ transferred more charges to the catalyst models with an increment in pyridinic-N atom number, resulting in the formation of active H species with higher electron deficiency. In contrast, in Fig. 8e and Fig. S18a2−c2, the more negative values of transferred Mulliken charges of C=O group in LA after adsorption due to the increased pyridinic-N atoms suggest that C=O becomes more electron-rich. This amplified electron density difference may facilitate electron transfer between active H atoms and C=O group of LA during the reaction, thereby enhancing the intrinsic activity of Ru@HNC. The correlations of TOFs~surface pyridinic-N/Ru^0 ratios and TOFs~Ru^0 3p$_{3/2}$ BEs, as depicted in Fig. 8f, demonstrate approximatively linear relationships, validating the electron-rich-Ru^0-induced activity promotion triggered by the increased surface pyridinic-N species resulting from the skillful formation of the yolk-shell structure and appropriate thinning of the carbon shell (Fig. 8g).

3.7. Stability of yolk-shell Ru@HNC and supported Ru/me-HNC

For the LA-to-GVL process, the traditional Ru/C bears a poor stability due to the tendency for easy aggregation and leaching of Ru [57]. Benefitting from the yolk-shell structure of Ru@HNC, the encapsulated Ru NPs possess the ability to restrain aggregation. Hence, cycling tests of yolk-shell Ru@*tk*-HNC, Ru@*me*-HNC, and Ru@*tn*-HNC were conducted, with supported Ru*me*-HNC and Ru/AC as references. As depicted in Fig. 9a, Ru@*me*-HNC can be reused for eight runs without significant activity decline (conversion > 89%), obviously outperforming Ru*me*-HNC and Ru/AC, highlighting the advantage of the yolk-shell structure in achieving good stability. Meanwhile, the activities of Ru@*tk*-HNC and Ru@*tn*-HNC noticeably decrease by the eighth (conversion = 65%) and fourth (conversion = 64%) cycles, respectively, both inferior to Ru@*me*-HNC, signifying the importance of shell thickness in maintaining good stability.

SEM images of Ru@*me*-HNC after seven runs (Fig. 9b and Fig. S19a) and Ru*me*-HNC after three runs (Fig. 9c and Fig. S19b) reveal partial damages to hollow nanospheres, especially for Ru@*me*-HNC after more
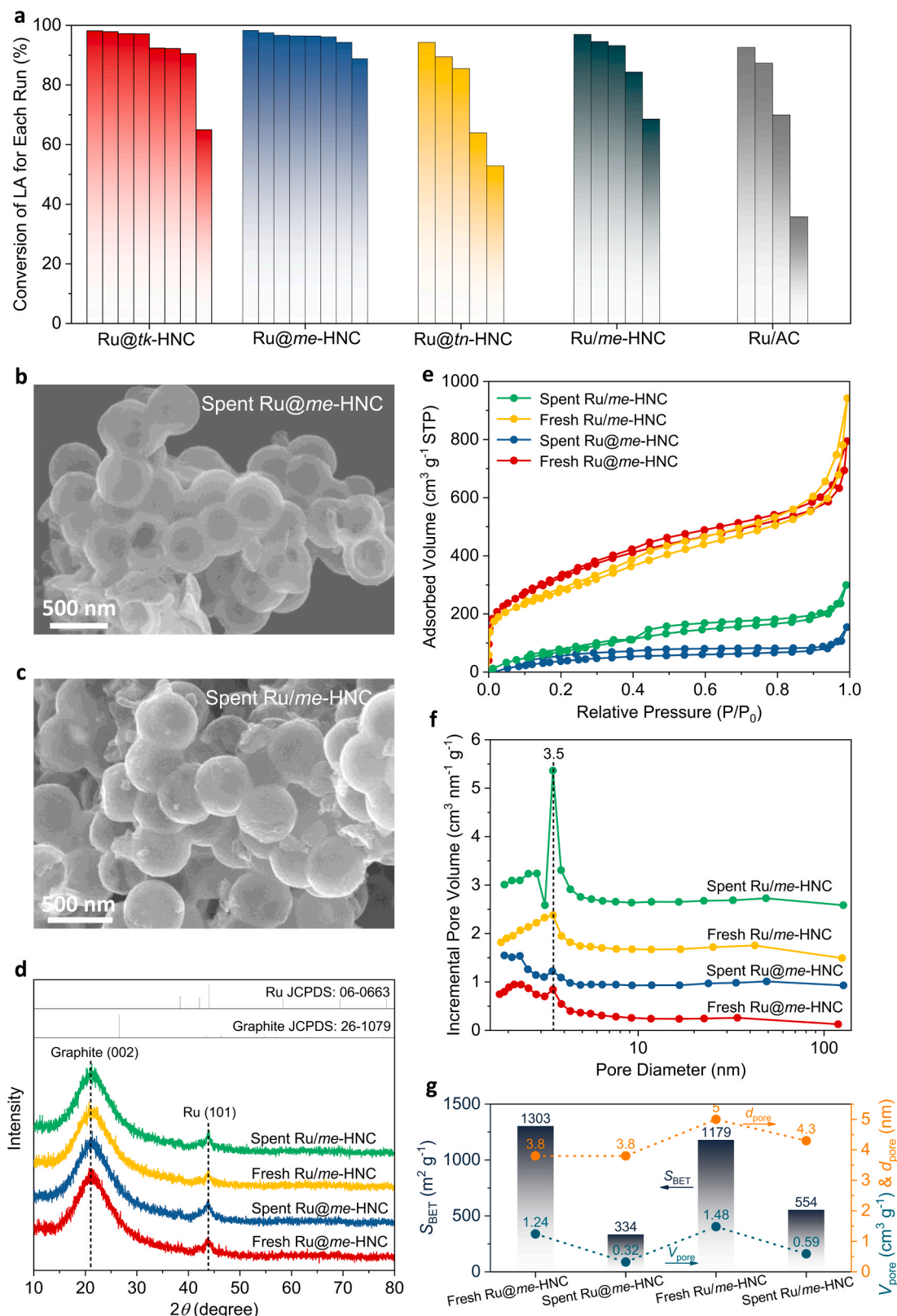
Fig. 9. (a) The stability of the as-synthesized Ru@*tk*-HNC, Ru@*me*-HNC, Ru@*tn*-HNC, Ru/*me*-HNC, and Ru/AC catalysts. Reaction conditions: 56 µmol of Ru (catalyst mass: 60.1, 58.8, 57.8, 58.8, and 58.8 mg for Ru@*tk*-HNC, Ru@*me*-HNC, Ru@*tn*-HNC, Ru/*me*-HNC, and Ru/AC, respectively), 10 mmol of LA, 20 mL of H_2O, temperature of 30 °C, H_2 pressure of 1.0 MPa, stirring rate of 1600 rpm, and reaction time of 3.5 h. For each reaction, the selectivity of GVL maintains at 99.9%; SEM images of (b) the Ru@*me*-HNC catalyst after seven catalytic runs (spent Ru@*me*-HNC) and (c) the Ru/*me*-HNC catalyst after three catalytic runs (spent Ru/*me*-HNC); (d) Power XRD patterns, (e) N_2 physisorption isotherms, (f) BJH pore size distributions based on the desorption isotherms, and (g) the corresponding physicochemical parameters of fresh and spent Ru@*me*-HNC and Ru/*me*-HNC catalysts.

cycles, accompanied by no significant change in crystal structure (Fig. 9d) and a slight decrease in d_{pore} (Fig. 9f and Fig. 9g) but dramatical declines in S_{BET} and V_{pore} compared to the corresponding fresh catalysts (Fig. 9e and Fig. 9g), which should be the primary reasons for the decline in activity.

The demonstrated enhancements in intrinsic catalytic activity and stability, ascribed to the distinctive structural design and surface chemistry, open avenues for exploring analogous strategies in other biomass upgrading and related processes. Further research could concentrate on expanding the scope of active metals to encompass non-noble metals, diversifying dopants and shell materials, investigating the scalability of the synthesis process, and continually advancing understanding of the catalytic mechanism at the atomic level. These endeavors will not only broaden the applicability of yolk-shell nanocatalysts, but also facilitate their integration into sustainable and scalable biomass conversion technologies.

4. Conclusions

In summary, yolk-shell electron-rich Ru@hollow pyridinic-N-doped carbon nanospheres with a controlled shell thickness ranging from 20 to 70 nm and an ultrahigh surface area of 4016 m^2 g^{-1} are successfully fabricated. In the LA-to-GVL process at 30 °C, the GVL selectivity remains at 99.9% regardless of the carbon shell thickness. The TOF of LA increases gradually with the thinning of the carbon shell, reaching a maximum of 18733.4 h^{-1} on Ru@*tn*-HNC with a shell thickness of 20 nm. Systematic characterizations, DFT simulations, Mulliken population analysis, and kinetics study confirm that such intrinsic activity enhancement originates from the formation of electron-rich Ru^0 and a positive shift of the *d*-band center towards the Fermi level due to the exposure of more surface pyridinic-N species through the skillful formation of the yolk-shell structure and appropriate thinning of the carbon shell. This results in suitably intensified Ru^0−H interaction, advantageous adsorption of reactants, facilitated electron transfer between active H and the C=O group of LA, and ultimately lower apparent activation energy. Approximately linear correlations between TOFs and surface pyridinic-N/Ru^0 ratios, as well as between TOFs and Ru^0 $3p_{3/2}$ binding energies, are demonstrated, validating the pivotal roles played by the unique yolk-shell structure and appropriate thinning of the carbon shell. Remarkably, outstanding stability for up to eight catalytic cycles is achieved on Ru@*me*-HNC with a shell thickness of 36 nm, and both this stability and its TOF significantly outperform conventionally externally-supported Ru/*me*-HNC and Ru/AC catalysts. These findings offer new insights for improving the intrinsic catalytic performances of metal nanocatalysts in biomass upgrading by designing yolk-shell nanostructures and precisely regulating the electronic and geometrical configurations of void-confined metal nanoparticles through engineering shell microenvironment, thereby holding potential in a wide range of application scenarios.

CRediT authorship contribution statement

Jingsong Yang: Writing – original draft, Visualization, Investigation, Formal analysis, Data curation. **Ruidong Shi:** Visualization, Validation, Investigation, Formal analysis, Data curation. **Xiaoxin Xu:** Validation, Data curation. **Yuanting Li:** Formal analysis. **Xue Wang:** Formal analysis. **Gongbing Zhou:** Writing – review & editing, Visualization, Supervision, Resources, Project administration, Methodology, Funding acquisition, Formal analysis, Data curation, Conceptualization.

Declaration of Competing Interest

The authors declare that they have no known competing financial interests or personal relationships that could have appeared to influence the work reported in this paper.

Data Availability

Data will be made available on request.

Appendix A. Supporting information

Supplementary data associated with this article can be found in the online version at doi:10.1016/j.apcatb.2024.124193.

References

[1] L.-S. Lin, J.B. Song, H.-H. Yang, X.Y. Chen, Yolk−shell nanostructures: Design, synthesis, and biomedical applications, Adv. Mater. 30 (2018) 1704639, https://doi.org/10.1002/adma.201704639.

[2] Z.H. Yu, N. Ji, J. Xiong, X.Y. Li, R. Zhang, L.D. Zhang, X.B. Lu, Ruthenium-nanoparticle-loaded hollow carbon spheres as nanoreactors for hydrogenation of levulinic acid: explicitly recognizing the void-confinement effect, Angew. Chem. Int. Ed. 60 (2021) 20786–20794, https://doi.org/10.1002/anie.202107314.

[3] Y.T. Pi, L.X. Cui, W.H. Luo, H.T. Li, Y.F. Ma, N. Ta, X.Y. Wang, R. Gao, D. Wang, Q.H. Yang, J. Liu, Design of hollow nanoreactors for size- and shape-selective catalytic semihydrogenation driven by molecular recognition, Angew. Chem. Int. Ed. 62 (2023) e202307096, https://doi.org/10.1002/anie.202307096.

[4] X.M. Ren, M. Guo, H. Li, C.B. Li, L. Yu, J. Liu, Q.H. Yang, Microenvironment engineering of ruthenium nanoparticles incorporated into silica nanoreactors for enhanced hydrogenations, Angew. Chem. Int. Ed. 58 (2019) 14483–14488, https://doi.org/10.1002/anie.201908602.

[5] Y. Yang, S.Y. Zhang, L. Gu, S. Shao, W. Li, D.H. Zeng, F. Yang, S.J. Hao, Stable yolk-structured catalysts towards aqueous levulinic acid hydrogenation within a single Ru nanoparticle anchored inside the mesoporous shell of hollow carbon spheres, J. Colloid Interf. Sci. 576 (2020) 394–403, https://doi.org/10.1016/j.jcis.2020.05.039.

[6] S. Xiong, R.D. Tang, D.X. Gong, Y.C. Deng, C.Y. Zhang, J.F. Zheng, M.E. Zhong, L. Su, L.H. Yang, C.J. Liao, Yolk-shell catalyst: from past to future, Appl. Mater. Today 21 (2020) 100798, https://doi.org/10.1016/j.apmt.2020.100798.

[7] Y.F. Ma, L.W. Wang, W.T. Zhao, T.Y. Liu, H.T. Li, W.H. Luo, Q.K. Jiang, W. Liu, Q.H. Yang, J. Huang, R.G. Zhang, J. Liu, G.Q.M. Lu, C. Li, Reactant enrichment in hollow void of Pt NPs@MnO$_x$ nanoreactors for boosting hydrogenation performance, Natl. Sci. Rev. 10 (2023) nwad201, https://doi.org/10.1093/nsr/nwad201.

[8] R.-P. Zhang, B.W. He, R.-P. Yang, Y.-X. Zhang, W.-C. Li, L.-H. Zhu, S.-J. Wang, D.-Q. Wang, X. Liu, L.W. Chen, C.-W. Wu, A.-H. Lu, Nanoengineered design of inside-heating hot nanoreactor surrounded by cool environment for selective hydrogenations, Adv. Mater. 35 (2023) 2302793, https://doi.org/10.1002/adma.202302793.

[9] D.L. Wang, C.H. Zhang, L.C. Zhang, X.B. Xie, Y. Lv, Integrated optimization of crystal facets and nanoscale spatial confinement toward the boosted catalytic performance of Pd nanocrystals, Inorg. Chem. 63 (2024) 1247–1257, https://doi.org/10.1021/acs.inorgchem.3c03635.

[10] Y.L. Xu, J.H. Zhang, P.X. Wang, Y.W. Fan, Y.F. Jiang, X.N. Duan, Y.Y. Li, J.S. Zhang, Highly efficient and stable Ni-based catalyst for selective conversion of biomass-derived aldehydes and ketones to primary amines, Chem. Eng. J. 480 (2024) 148175, https://doi.org/10.1016/j.cej.2023.148175.

[11] C. Dong, Q. Yu, R.-P. Ye, P.P. Su, J. Liu, G.-H. Wang, Hollow carbon sphere nanoreactors loaded with PdCu nanoparticles: Void-confinement effects in liquid-phase hydrogenations, Angew. Chem. Int. Ed. 59 (2020) 18374–18379, https://doi.org/10.1002/anie.202007297.

[12] M. Kosari, S. Askari, A.M. Seayad, S.B. Xi, S. Kawi, A. Borgna, H.C. Zeng, Strong coke-resistivity of spherical hollow Ni/SiO$_2$ catalysts with shell-confined high-content Ni nanoparticles for methane dry reforming with CO$_2$, Appl. Catal. B: Environ. 310 (2022) 121360, https://doi.org/10.1016/j.apcatb.2022.121360.

[13] Z. Hu, M.M. Han, C. Chen, Z.D. Zou, Y. Shen, Z. Fu, X.G. Zhu, Y.X. Zhang, H.M. Zhang, H.J. Zhao, G.Z. Wang, Hollow carbon sphere encapsulated nickel nanoreactor for aqueous-phase hydrogenation-rearrangement tandem reaction with enhanced catalytic performance, Appl. Catal. B: Environ. 306 (2022) 121140, https://doi.org/10.1016/j.apcatb.2022.121140.

[14] Z.K. Peng, H.Y. Wang, L.L. Zhou, Y.B. Wang, J. Gao, G.J. Liu, S.A.T. Redfern, X.L. Feng, S.Y. Lu, B.J. Li, Z.Y. Liu, Hollow carbon shells enhanced by confined

ruthenium as cost-efficient and superior catalysts for the alkaline hydrogen evolution reaction, J. Mater. Chem. A 7 (2019) 6676–6685, https://doi.org/10.1039/C8TA09136F.

[15] J.J. Pei, L. Yang, J. Lin, Z.D. Zhang, Z.Y. Sun, D.S. Wang, W.X. Chen, Integrating host design and tailored electronic effects of yolk−shell Zn−Mn diatomic sites for efficient CO₂ electroreduction, Angew. Chem. Int. Ed. 63 (2024) e20231612, https://doi.org/10.1002/anie.202316123.

[16] L.Z. Meng, J.H. Wang, J.Y. Qi, X.L. Liu, L. Li, J.N. Yun, G. Wang, J.F. Yan, J.T. Bai, Yolk-shell construction of Co₀.₇Fe₀.₃ modified with dual carbon for broadband microwave absorption, J. Colloid Interf. Sci. 659 (2024) 945–958, https://doi.org/10.1016/j.jcis.2024.01.052.

[17] X.L. Jia, D.H. Guo, Z.L. Wang, N. Zhou, R.Z. Jin, B.S. Xu, Synthesis of Co@N-doped carbon with yolk−shell heterostructures for efficient electromagnetic wave absorption, J. Alloy Compd. 987 (2024) 174185, https://doi.org/10.1016/j.jallcom.2024.174185.

[18] S.G. Gao, L. Zhang, H.T. Yu, H.Q. Wang, Z.W. He, K. Huang, Palladium-encapsulated hollow porous carbon nanospheres as nanoreactors for highly efficient and size-selective catalysis, Carbon 175 (2021) 307–311, https://doi.org/10.1016/j.carbon.2021.01.023.

[19] H. Wu, F.Z. Huang, B.J. Wang, S.P. Wang, W.B. Nie, S.K. Li, F.H. Liu, H. Zhang, Decorating CoNi alloy-encapsulated carbon nanotube hollow nanocages to enable dielectric loss for highly efficient microwave absorption, ACS Appl. Nano Mater. 5 (2022) 13187–13197, https://doi.org/10.1021/acsanm.2c02928.

[20] H. Tian, X.Y. Liu, L.B. Dong, X.M. Ren, H. Liu, C.A.H. Price, Y. Li, G.X. Wang, Q. H. Yang, J. Liu, Enhanced hydrogenation performance over hollow structured Co-CoOₓ@N-C capsules, Adv. Sci. 6 (2019) 1900807, https://doi.org/10.1002/advs.201900807.

[21] D.-S. Bin, Z.-X. Chi, Y.T. Li, K. Zhang, X.Z. Yang, Y.-G. Sun, J.-Y. Piao, A.-M. Cao, L.-J. Wan, Controlling the compositional chemistry in single nanoparticles for functional hollow carbon nanospheres, J. Am. Chem. Soc. 139 (2017) 13492–13498, https://doi.org/10.1021/jacs.7b07027.

[22] Y.F. Zhang, Y. Shen, Electrochemical hydrogenation of levulinic acid, furfural and 5-hydroxymethylfurfural, Appl. Catal. B: Environ. 343 (2024) 123576, https://doi.org/10.1016/j.apcatb.2023.123576.

[23] Y.W. Lu, Y.X. Wang, Q.H. Tang, Q. Cao, W.H. Fang, Synergy in Sn-Mn oxide boosting the hydrogenation catalysis of supported Pt nanoparticles for selective conversion of levulinic acid, Appl. Catal. B Environ. 300 (2022) 120746, https://doi.org/10.1016/j.apcatb.2021.120746.

[24] G.J. Lan, Z.Q. Li, Xi.J. Han, L.P. Zhang, Y.Y. Qiu, X.C. Sun, Z.Z. Cheng, Y. Li, Modulating the surface structure of nanodiamonds to enhance the electronic metal−support interaction of efficient ruthenium catalysts for levulinic acid hydrogenation, N. J. Chem. 47 (2023) 6258–6265, https://doi.org/10.1039/D2NJ06229A.

[25] S.S. Wang, Z.W. Zhuang, X. Chen, Y. Wang, X.X. Li, M.D. Yang, Y.L. Wu, Q. Peng, C. Chen, Y.D. Li, 3D oxide-derived Ru catalyst for ultra-efficient hydrogenation of levulinic acid to γ-valerolactone, Small 20 (2024) 2306227, https://doi.org/10.1002/smll.202306227.

[26] W.Y. Liang, G.Y. Xu, X. Zhang, H.Y. Chen, Y. Fu, MFI zeolite with confined adjustable synergistic Cu sites for the hydrogenation of levulinic acid, Green. Chem. 26 (2024) 498–506, https://doi.org/10.1039/D3GC03356B.

[27] S. Dutta, I.K.M. Yu, D.C.W. Tsang, Y.H. Ng, Y.S. Ok, J. Sherwood, J.H. Clark, Green synthesis of gamma-valerolactone (GVL) through hydrogenation of biomass-derived levulinic acid using non-noble metal catalysts: a critical review, Chem. Eng. J. 372 (2019) 992–1006, https://doi.org/10.1016/j.cej.2019.04.199.

[28] S. Shao, Z.Z. Ding, C.L. Shang, S.Y. Zhang, Y.C. Ke, G.L. Zhu, Y. Yang, Yolk-shell Co catalysts with controlled nanoparticle/single-atom ratio for aqueous levulinic acid hydrogenation to γ-valerolactone, Chem. Eng. J. 450 (2022) 138153, https://doi.org/10.1016/j.cej.2022.138153.

[29] R.Q. Raguindin, B.Z. Desalegn, M.N. Gebresillase, J.G. Seo, Yolk-shell nickel−cobalt phosphides as bifunctional catalysts in the solvent-free hydrogenation of levulinic acid to gamma-valerolactone, Renew. Energ. 191 (2022) 763–774, https://doi.org/10.1016/j.renene.2022.04.078.

[30] Y. Yang, F. Yang, H. Wang, B. Zhou, S.J. Hao, Amine-promoted Ru₁/Fe₃O₄ encapsulated in hollow periodic mesoporousorganosilica sphere as a highly selective and stable catalyst for aqueous levulinic acid hydrogenation, J. Colloid Interf. Sci. 581 (2021) 167–176, https://doi.org/10.1016/j.jcis.2020.07.114.

[31] Z.-L. Yu, Y.-C. Gao, B. Qin, Z.-Y. Ma, S.-H. Yu, Revitalizing traditional phenolic resin toward a versatile platform for advanced materials, Acc. Mater. Res. 5 (2024) 146–159, https://doi.org/10.1021/accountsmr.3c00194.

[32] Z.Q. Li, C.J. Lu, Z.P. Xia, Y. Zhou, Z. Luo, X-ray diffraction patterns of graphite and turbostratic carbon, Carbon 45 (2007) 1686–1695, https://doi.org/10.1016/j.carbon.2007.03.038.

[33] E.D. Obraztsova, M. Fujii, S. Hayashi, V.L. Kuznetsov, Y.V. Butenko, A.L. Chuvilin, Raman identification of onion-like carbon, Carbon 36 (1998) 821–826, https://doi.org/10.1016/S0008-6223(98)00014-1.

[34] C. Kim, S.-H. Park, J.-I. Cho, D.-Y. Lee, T.-J. Park, W.-J. Lee, K.-S. Yang, Raman spectroscopic evaluation of polyacrylonitrile-based carbon nanofibers prepared by electrospinning, J. Raman Spectrosc. 35 (2004) 928–933, https://doi.org/10.1002/jrs.1233.

[35] F. Xu, Z.W. Tang, S.Q. Huang, L.Y. Chen, Y.R. Liang, W.C. Mai, H. Zhong, R.W. Fu, D.C. Wu, Facile synthesis of ultrahigh-surface-area hollow carbon nanospheres for enhanced adsorption and energy storage, Nat. Commun. 6 (2015) 7221, https://doi.org/10.1038/ncomms8221.

[36] X.Y. Liu, L.H. Gong, L.W. Wang, C.Q. Chang, P.P. Su, Y.H. Dou, S.X. Dou, Y. Li, F. L. Gong, J. Liu, Enabling ultrafine Ru nanoparticles with tunable electronic structures via a double-shell hollow interlayer confinement strategy toward

[37] X.Y. Liu, G.J. Lan, Y. Boyjoo, L.H. Qian, S. Gu, C.A.H. Price, L. Wang, Y. Li, J. Liu, N-doped carbon spheres impregnated with highly monodispersed ruthenium nanoparticles as a hydrogenation catalyst, Chem. Eng. J. 374 (2019) 895–903, https://doi.org/10.1016/j.cej.2019.05.213.

[38] X.Y. Liu, S. Ye, G.J. Lan, P.P. Su, X.L. Zhang, C.A.H. Price, Y. Li, J. Liu, Atomic pyridinic nitrogen sites promoting levulinic acid hydrogenations over double-shelled hollow Ru/C nanoreactors, Small 17 (2021) 2101271, https://doi.org/10.1002/smll.202101271.

[39] K. Mori, K. Miyawaki, H. Yamashita, Ru and Ru−Ni nanoparticles on TiO₂ support as extremely active catalysts for hydrogen production from ammonia−borane, ACS Catal. 6 (2016) 3128–3135, https://doi.org/10.1021/acscatal.6b00715.

[40] Y.S. Li, J.L. Shi, Hollow-structured mesoporous materials: Chemical synthesis, functionalization and applications, Adv. Mater. 26 (2014) 3176–3205, https://doi.org/10.1002/adma.201305319.

[41] J.S. Yang, R.D. Shi, G.B. Zhou, Selective hydrogenation of levulinic acid at room temperature: Boosting ruthenium nanoparticle efficiency via coupling with *in-situ* pyridinic-N-doped carbon nanoflowers, Chem. Eng. J. 475 (2023) 146297, https://doi.org/10.1016/j.cej.2023.146297.

[42] J.F. Moulder, W.F. Stickle, P.E. Sobol, K.D. Bomben, Handbook of X-ray Photoelectron Spectroscopy, Perkin-Elmer, Minnesota, 1992.

[43] Q.-Y. Bi, J.-D. Lin, Y.-M. Liu, H.-Y. He, F.-Q. Huang, Y. Cao, Dehydrogenation of formic acid at room temperature: Boosting palladium nanoparticle efficiency by coupling with pyridinic-nitrogen-doped carbon, Angew. Chem. Int. Ed. 55 (2016) 11849–11853, https://doi.org/10.1002/anie.201605961.

[44] W.Z. Shen, W.B. Fan, Nitrogen-containing porous carbons: Synthesis and application, , J. Mater. Chem. A 1 (2013) 999–1013, https://doi.org/10.1039/C2TA00028H.

[45] X.G. Li, Q.L. Yao, Z.B. Li, H.B. Li, Q.-L. Zhu, Z.-H. Lu, Porphyrin framework-derived N-doped porous carbon-confined Ru for NH₃BH₃ methanolysis: the more pyridinic-N, the better, J. Mater. Chem. A 10 (2022) 326–336, https://doi.org/10.1039/D1TA06807E.

[46] P.C.H. Mitchell, C.E. Scott, J.-P. Bonnelle, J.G. Grimblot, Ru/alumina and Ru-Mo/alumina catalysts: An XPS study, J. Catal. 107 (1987) 482–489, https://doi.org/10.1016/0021-9517(87)90312-5.

[47] W.J. Song, Z. Chen, W.K. Lai, I. Rodríguez-Ramos, X.D. Yi, W.Z. Weng, W.P. Fang, Effect of lanthanum promoter on the catalytic performance of levulinic acid hydrogenation over Ru/carbon fiber catalyst, Appl. Catal. A Gen. 540 (2017) 21–30, https://doi.org/10.1016/j.apcata.2017.04.004.

[48] E. Gallegos-Suárez, A. Guerrero-Ruiz, I. Rodríguez-Ramos, Efficient hydrogen production from glycerol by steam reforming with carbon supported ruthenium catalysts, Carbon 96 (2016) 578–587, https://doi.org/10.1016/j.carbon.2015.09.112.

[49] X.J. Cui, A.-E. Surkus, K. Junge, C. Topf, J. Radnik, C. Kreyenschulte, M. Beller, Highly selective hydrogenation of arenes using nanostructured ruthenium catalysts modified with a carbon−nitrogen matrix, Nat. Commun. 7 (2016) 11326, https://doi.org/10.1038/ncomms11326.

[50] G. Wang, L.C. Sun, W.Y. Liu, H.J. Zhan, S.X. Bi, Iron-nickel alloy particles with N-doped carbon "armor" as a highly selective and long-lasting catalyst for the synthesis of N-benzylaniline molecules, Nano Res 16 (2023) 1–12, https://doi.org/10.1007/s12274-023-6041-z.

[51] H.H. Veisi, M. Akbari, B. Karimi, H. Vali, R. Luque, One-pot acid−base catalysed tandem reactions using a bimodal N, S-doped cubic mesoporous carbon, Green. Chem. 25 (2023) 4076–4089, https://doi.org/10.1039/D3GC00117B.

[52] Z.Z. Liu, X.Y. Gao, G.Y. Song, Synergy of ultra-low-loaded ruthenium with alumina stimulating the catalytic hydrogenation of levulinic acid into γ-valerolactone, Chem. Eng. J. 470 (2023) 143869, https://doi.org/10.1016/j.cej.2023.143869.

[53] S. Shao, Y. Yang, K.J. Sun, S.T. Yang, A. Li, F. Yang, X.R. Luo, S.J. Hao, Y.C. Ke, Electron-rich ruthenium single-atom alloy for aqueous levulinic acid hydrogenation, ACS Catal. 11 (2021) 12146–12158, https://doi.org/10.1021/acscatal.1c03004.

[54] B.Y. Li, H.C. Zhao, J. Fang, J.F. Li, W. Gao, K.X. Ma, C. Liu, H.R.Y. Yang, X.G. Ren, Z.P. Dong, Ru nanoparticles anchored on porous N-doped carbon nanospheres for efficient catalytic hydrogenation of Levulinic acid to γ-valerolactone under solvent-free conditions, J. Colloid Interf. Sci. 623 (2022) 905–914, https://doi.org/10.1016/j.jcis.2022.05.017.

[55] Y.H. Han, J. Dai, R.R. Xu, W.Y. Ai, L.R. Zheng, Y. Wang, W.S. Yan, W.X. Chen, J. Luo, Q. Liu, D.S. Wang, Y.D. Li, Notched-polyoxometalate strategy to fabricate atomically dispersed Ru catalysts for biomass conversion, ACS Catal. 11 (2021) 2669–2675, https://doi.org/10.1021/acscatal.0c04006.

[56] X.Y. Liu, G.J. Lan, P.P. Su, L.H. Qian, T.R. Reina, L. Wang, Y. Li, J. Liu, Highly stable Ru nanoparticles incorporated in mesoporous carbon catalysts for production of γ-valerolactone, Catal. Today 351 (2020) 75–82, https://doi.org/10.1016/j.cattod.2018.12.039.

[57] Y. Yang, G. Gao, X. Zhang, F.W. Li, Facile fabrication of composition-tuned Ru–Ni bimetallics in ordered mesoporous carbon for levulinic acid hydrogenation, ACS Catal. 4 (2014) 1419–1425, https://doi.org/10.1021/cs401030u.

[58] O. Mamun, M. Saleheen, J.Q. Bond, A. Heyden, Investigation of solvent effects in the hydrodeoxygenation of levulinic acid to γ-valerolactone over Ru catalysts, J. Catal. 379 (2019) 164–179, https://doi.org/10.1016/j.jcat.2019.09.026.

[59] J.J. Tan, J.L. Cui, T.S. Deng, X.J. Cui, G.Q. Ding, Y.L. Zhu, Y.W. Li, Water-promoted hydrogenation of levulinic acid to γ-valerolactone on supported ruthenium catalyst, ChemCatChem 7 (2015) 508–512, https://doi.org/10.1002/cctc.201402834.

[60] A.S. Piskun, H.H. van de Bovenkamp, C.B. Rasrendra, J.G.M. Winkelman, H. J. Heeres, Kinetic modeling of levulinic acid hydrogenation to γ-valerolactone in water using a carbon supported Ru catalyst, Appl. Catal. A: Gen. 525 (2016) 158–167, https://doi.org/10.1016/j.apcata.2016.06.033.

[61] O.A. Abdelrahman, A. Heyden, J.Q. Bond, Analysis of kinetics and reaction pathways in the aqueous-phase hydrogenation of levulinic acid to form γ-valerolactone over Ru/C, ACS Catal. 4 (2014) 1171–1181, https://doi.org/10.1021/cs401177p.

[62] S. Cao, J.R. Monnier, C.T. Williams, W.J. Diao, J.R. Regalbuto, Rational nanoparticle synthesis to determine the effects of size, support, and K dopant on Ru activity for levulinic acid hydrogenation to γ-valerolactone, J. Catal. 326 (2015) 69–81, https://doi.org/10.1016/j.jcat.2015.03.004.

[63] W.J. Song, M.C. Lozano-Martin, E. Gallegos-Suarez, C. Ramirez-Barria, W.Z. Weng, X.D. Yi, B. Bachiller-Baeza, A. Guerrero-Ruiz, I. Rodriguez-Ramos, New insights in the development of carbon supported ruthenium catalysts for hydrogenation of levulinic acid, Curr. Catal. 7 (2018) 129–137, https://doi.org/10.2174/2211544707666180328162825.

[64] J.F. Zhang, P. Zhou, J.J. Liu, J.G. Yu, New understanding of the difference of photocatalytic activity among anatase, rutile and brookite TiO_2, Phys. Chem. Chem. Phys. 16 (2014) 20382–20386, https://doi.org/10.1039/C4CP02201G.

[65] J.K. Nørskov, F. Studt, F. Abild-pedersen, T. Bligaard, Fundamental Concepts in Heterogeneous Catalysis, John Wiley & Sons, New Jersey, 2015.